Identification of high sugar diet-induced dysregulated metabolic pathways in muscle using tissue-specific metabolic models in *Drosophila*

Authors

Sun Jin Moon[1*], Yanhui Hu[1], Monika Dzieciatkowska[2], Ah-Ram Kim[1], Po-Lin Chen[1], John M. Asara[3,4], Angelo D'Alessandro[2], Norbert Perrimon[1,5*]

Affiliations

[1]Department of Genetics, Blavatnik Institute, Harvard Medical School, Boston, MA 02115

[2]Department of Biochemistry and Molecular Genetics, Anschutz Medical Campus, University of Colorado School of Medicine, Aurora, CO 80045

[3]Division of Signal Transduction, Beth Israel Deaconess Medical Center, Boston, MA 02115

[4]Department of Medicine, Harvard Medical School, Boston, MA 02115

[5]Howard Hughes Medical Institute, Harvard Medical School, Boston, MA 02115

[*]Correspondence: Sun Jin Moon and Norbert Perrimon

Emails**:** sunjin_moon@hms.harvard.edu and perrimon@genetics.med.harvard.edu

Abstract

Individual tissues perform highly specialized metabolic functions to maintain whole-body homeostasis. Although *Drosophila* serves as a powerful model for studying human metabolic diseases, a lack of tissue-specific metabolic models makes it challenging to quantitatively assess the metabolic processes of individual tissues and disease models in this organism. To address this issue, we reconstructed 32 tissue-specific genome-scale metabolic models (GEMs) using pseudo-bulk single cell transcriptomics data, revealing distinct metabolic network structures across tissues. Leveraging enzyme kinetics and flux analyses, we predicted tissue-dependent metabolic pathway activities, recapitulating known tissue functions and identifying tissue-specific metabolic signatures, as supported by metabolite profiling. Moreover, to demonstrate the utility of tissue-specific GEMs in a disease context, we examined the effect of a high sugar diet (HSD) on muscle metabolism. Together with ^{13}C-glucose isotopic tracer studies, we identified glyceraldehyde 3-phosphate dehydrogenase (GAPDH) as a rate-limiting enzyme in response to HSD. Mechanistically, the decreased GAPDH activity was linked to elevated NADH/NAD^+ ratio, caused by disturbed NAD^+ regeneration rates, and oxidation of GAPDH. Furthermore, we introduced a pathway flux index to predict and validate additionally perturbed pathways, including fructose and butanoate metabolism. Altogether, our results represent a significant advance in generating quantitative tissue-specific GEMs and flux analyses in *Drosophila*, highlighting their use for identifying dysregulated metabolic pathways and their regulation in a human disease model.

Highlights

- Reconstruction of tissue-specific genome-scale metabolic models in *Drosophila*
- Quantitative metabolic network and flux analyses reveal tissue-dependent metabolic pathway activities
- ^{13}C-isotope tracing and flux analysis identify GAPDH as a rate-limiting enzyme in muscle in response to HSD
- Increased NADH/NAD$^+$ ratio and oxidation of GAPDH in muscle under HSD
- Pathway flux index analysis predicts altered fructose and butanoate metabolism in muscle in response to HSD

Keywords

Tissue metabolism, genome-scale metabolic model, flux balance analysis, ^{13}C isotope tracing, GAPDH, NADH/NAD$^+$, high sugar diet, *Drosophila*

Introduction

Complex multicellular organisms have tissue-specific metabolic networks that support highly specialized tissue functions[1]. These networks not only modulate intracellular metabolic pathway activities to meet their unique metabolic demands, but also enable dynamic communication among tissues through metabolites, allowing the organism to respond to environmental changes[2,3]. Furthermore, both tissues and their interaction with the environment influence tissue-specific metabolic phenotypes. Delineating this complexity is crucial to understand how tissue-specific metabolic activities contribute to whole-body metabolic homeostasis and how metabolic dysregulation leads to disease.

The high conservation of metabolic genes and functionally analogous organs between humans and fruit flies, together with the short generation time, lifespan, and availability of numerous genetic and analytical tools for *Drosophila*, has made flies an excellent organism in which to model human metabolic diseases[4,5]. Indeed, many mechanisms underlying dysregulated metabolism associated with type 2 diabetes[6,7], aging[8], and cancer[9] at both the organelle and tissue levels[10] have been elucidated in flies. Furthermore, advances in analytical tools such as mass spectrometry have allowed quantification of hundreds of metabolites, providing systems-level understanding in response to tissue-specific genetic perturbations or nutritional interventions[11,12]. However, as metabolite profiling analyses are generally performed at the whole-organism level, tissue-specific metabolic information is often missing, underscoring the need for methods for interrogation of metabolism at a tissue-specific level.

For tissue-specific metabolic investigation, biosensors and mass spectrometry-based analyses have been widely applied. While biosensors can be expressed in a specific tissue using the Gal4-UAS system to record metabolite dynamics, these sensors target specific analytes, preventing a system-level analysis of the metabolome[13]. Alternatively, individual tissues can be dissected and mass spectrometry applied to identify changes in hundreds of metabolites in each tissue[14]. However, dissecting individual tissues is often difficult due to their small sizes. Further, the extended time required for dissection may cause artefacts in metabolite pools with high rates of turnover[15]. Moreover, as metabolites are linked to various enzymatic reactions, analysis of metabolites alone make it difficult to evaluate metabolic pathway activities in a complex biochemical architecture[16].

To quantitatively evaluate metabolic networks and pathway activities, genome-scale metabolic models (GEMs) and flux balance analysis have been widely used[17]. GEMs are mathematical models that represent the stoichiometry of biochemical reactions[18]. GEMs can be improved through integration of transcriptomics or proteomics datasets with generic models, generating context-specific GEMs[19–21]. Based on the curated models, a variety of computational analyses and simulations can be implemented to predict

individual reaction rates, identify perturbed metabolites and genes associated with diseases, and determine the essential substrates that contribute to cellular phenotypes[22]. In *Drosophila,* several GEMs have been generated to analyze metabolic perturbations in silico. For instance, FlySilico was developed to identify essential amino acids that control larval growth rate[23] and iDrosophila was built to evaluate a fly model of Parkinson's disease [24]. Moreover, Fruitfly1 was reconstructed as a comprehensive generic model based on ortholog and biochemical reactions from the KEGG database[25]. Although these *Drosophila* GEMs enabled quantitative metabolic network evaluation under specific conditions, such models do not represent the resolution of tissue-level metabolism analyses at the level of the whole organism.

Complementary to genome-scale model-based flux balance analysis, the use of ^{13}C isotope tracers and subsequent metabolic flux analyses[26] have served as powerful tools to interrogate cellular metabolism that is differentially activated in models of diseases such as cancer[27–29], obesity[30,31], and diabetes[32]. For example, in *Drosophila*, ^{13}C isotope tracers have been used to reveal roles for cysteine metabolism in autophagy during fasting[33], lactate derived from the gut in regulating behavior[34], and methionine degradation pathway activities during aging[35]. Although evaluation of *in vivo* metabolic flux based on isotopologues of the ^{13}C isotope can be challenging due to the complexities derived from exchange rates, fractional enrichment data indirectly provides information on pathway activities. Together with GEMs, ^{13}C isotope tracer-based studies can lead to a more comprehensive and quantitative metabolic analyses. Currently, such integrated and quantitative analyses have been lacking for the study of metabolism in *Drosophila*.

Here, we addressed these unmet needs by developing tissue-specific GEMs for adult flies using pseudo-bulk single cell transcriptomics data. Using the resulting tissue-specific GEMs, we evaluated the metabolic network structures and differential reaction contents of individual tissues. Furthermore, we performed flux balance, variability, and pathway analyses to predict fluxes across tissues, while validating our predictions with available information in the literature and newly generated data on metabolite profiles. Moreover, to demonstrate the utility of tissue-specific GEMs for the study of human metabolic diseases, we evaluated the effects of a high sugar diet (HSD) on muscle metabolism. Using our muscle-GEM and ^{13}C-glucose glucose tracers, we identified glyceraldehyde 3-phosphate dehydrogenase (GAPDH) as a rate-limiting enzyme in glycolysis. Finally, we present a pathway flux index analysis that predicted HSD-induced dysregulated pathways.

Results

Reconstruction of tissue-specific metabolic models reveals distinct metabolic network structures and pathway coverage

We developed a pipeline to reconstruct tissue-specific GEMs using pseudo-bulk single-nuclei gene expression data, and subsequently analyzed their metabolic network structures, subsystem coverage and functions (**Fig. 1a**). First, we used Fruitfly1 as the basic GEM because this generic model was most comprehensive regarding the coverage of reactions, metabolites, and genes compared to alternatives such as FlySilico or iDrosophila1[23,25]. Next, we manually curated this generic model by adding genes and EC numbers and assigned it as Fruitfly3 (see Methods). Using this GEM, we used task-driven model reconstruction algorithm (tINIT)[36] to integrate pseudo-bulk single-nuclei RNA sequencing (snRNAseq) data from Fly Cell Atlas[37], generating tissue-specific GEMs. Subsequently, we evaluated metabolic network structures by comparing the number of reactions, metabolites, and genes across the GEMs **(Supplementary fig. 1a).** Visualization of the relationships across the reaction structures of individual tissues revealed that tissues of similar types grouped together **(Fig. 1b and Supplementary fig. 1b)**. Notably, metabolic networks of muscle, fat body, gut, neurons, glial cells formed distinct clusters, while sub-types showed similarities within their respective groups.

Next, we evaluated metabolic pathway coverage by comparing the number of reactions in each metabolic subsystem across tissues **(Fig. 1c)**. We identified significant variation in 34 of 145 subsystems, with fat body and oenocytes containing a greater number of reactions associated with fatty acid oxidation pathways, including mitochondrial and peroxisomal beta-oxidation of unsaturated, even-chain, and odd-chain fatty acids. Moreover, we conducted a metabolic task analysis to assess the capability of the GEMs to complete 256 metabolic processes, including gluconeogenesis and cofactor de novo synthesis[38]. The analysis revealed that germline cells, male accessory glands, and the fat body were able to complete greater number of metabolic tasks than other tissues (**Fig. 1d and supplementary fig. 1c)**.

Additionally, as muscle, fat body, gut, glia, and neuron revealed distinct metabolic structures, we further investigated their metabolic subsystem coverage (**Supplementary fig. 1d)**. Of these tissues, muscle contained a greater number of reactions in pathways, including protein degradation and lipoic acid metabolism (**Supplementary fig. 1e)**. Although muscle is known to be a major site of protein synthesis and degradation[39], our analysis suggested that lipoic acid, an essential cofactor for mitochondrial metabolism and a precursor for antioxidant molecule, may be an important metabolism in muscle[40]. Furthermore, we found that certain tissues, such as subtypes of follicle cells, muscle, and multi-dendritic neurons contained a higher number of reactions that are described as extracellular transport reactions,

suggesting that these tissues might have higher metabolites transport across tissues **(Supplementary fig. 1f)**. Altogether, our reconstruction of tissue-specific GEMs and subsequent analyses demonstrate distinct tissue-specific metabolic network structures and their pathway coverage, confirming some previously reported functions and additionally providing insights into tissue-specific metabolic pathways.

Integration of enzyme kinetics and abundances reveals tissue-specific maximum rate distributions

Determining the maximum reaction rate or V_{max} can be useful not only in constraining the upper limits of individual reactions to enable more accurate flux predictions in GEMs[41], but also in estimating which tissues involve reactions that achieve higher rate capacity. To calculate maximum rates, we used available enzyme turnover number or k_{cat} and available enzyme abundance using an enzyme abundance prediction pipeline[42] **(Fig. 2a)**. In brief, the enzyme abundance prediction pipeline uses an ordinary differential equation to calculate the enzyme abundance, given the rate of protein translation, degradation, and mRNA levels (see Methods)[43] **(Supplementary Fig. 2a)**. Using mRNA levels from whole adult fly, we tested the pipeline and determined similar correlation patterns between the experimentally measured and predicted enzyme abundance values (with a difference in correlation of 0.12) **(Supplementary Fig. 2b – d)**. Next, we obtained experimentally k_{cat} values from the BRENDA database (see Methods, **Supplementary Fig. 2e - h**)[44]. Subsequently, we calculated V_{max} using a generalized equation of $V_{max} = k_{cat}[Enzyme]_T$ and found that nearly 92 % of the maximum rates were within the default maximum values set in the Fruitfly1, with the median V_{max} of 23.5 mmol/g-DCW/hr **(Supplementary Fig. 2i)**. Moreover, gene ontology analysis revealed that enzymes with higher maximum rates were involved in carboxylic acid metabolic processes, whereas enzymes with relatively slower maximum rates were involved in methylation and alkylation, confirming previously reported differences in the estimated rates of these metabolic processes[45] **(Supplementary Fig. 2j)**.

Next, we assessed V_{max} across individual tissues using the above pipeline with pseudo-bulk single nuclei gene expression data. We found that the fat body contained reactions that had the highest median V_{max} compared to other tissues **(Fig. 2b and supplementary Fig. 2k)**. Although a wide distribution of V_{max} values was predicted across reactions and tissues, median values were within the same order of magnitude across tissues (**supplementary Fig. 2l).** Furthermore, to determine whether tissues with higher V_{max} would complete more metabolic tasks than those with lower values, we compared V_{max} values with tissues' ability to complete metabolic tasks. We found that certain tissues such as fat body, oenocyte, hemocyte, germline, and escort cells were predicted to have both enzymes with higher V_{max} and the ability

to complete more metabolic tasks **(Fig 2c)**. Altogether, integration of enzyme k_{cat} and abundances revealed the distribution of maximum reaction rates in individual tissues and demonstrated that certain tissues with higher V_{max} were also capable of completing more metabolic tasks than those with lower V_{max}.

Pathway flux variability highlights tissue-dependent metabolic similarities and differences

To evaluate the flux distributions across tissues, we conducted a series of flux analyses, including flux balance analysis[17], flux variability analysis[46], and our pathway flux analysis (see Methods) **(Fig. 3a)**. As tissues share core metabolic objectives, such as maintaining NAD(P)H redox balance and ATP metabolism for survival[2], we set a common objective function, which was to maximize the production of NADPH, ATP, and NAD^+. The flux balance analysis revealed a wide variation of fluxes across tissues in core metabolic subsystems such as glycolysis, the TCA cycle, fatty acid oxidation, and NADPH metabolism **(supplementary fig. 3a)**. To evaluate which reactions vary most significantly in individual metabolic pathways across tissues, we calculated a coefficient of variation of each reaction in major metabolic pathways **(supplementary fig. 3b)**. In glycolysis, we found that the hexokinase rate was predicted to vary most significantly across tissues. Enzymes encoded by *Atpcl*, *Whd*, *Desat1/2*, or *Men,* which are categorized in distinct metabolic pathways*,* were also estimated to vary greatly across tissues, suggesting potentially differential metabolic regulation by these enzymes.

Next, we performed a flux variability analysis to determine the range of individual reaction rates when tissues were generating ATP, NAD^+, and NADPH at 90 %, compared to the optimized rates obtained from flux balance analysis. This analysis predicts tissues that carry greater flux range in individual enzymes, which could not be analyzed solely from flux balance analysis. For hexokinase, oenocytes was predicted to carry a greater flux range than other tissues **(Supplementary fig. 3c)**. On the other hand, for ATP citrate synthase, a key step in fatty acid synthesis, the fat body was predicted to show a greater range of flux range **(Supplementary fig. 3d)**. For carnitine palmitoyl-transferase 1, CNS surface-associated glial cells showed a greater flux range compared to other tissues **(Supplementary fig. 3e)**. In cytosolic NADPH metabolism, fatty acids desaturases, encoded by *Desat1/2*, showed greater variation across tissues, with oenocytes, fat body, and subtypes of neurons and glia showing greater flux ranges **(Supplementary fig. 3f)**. In mitochondrial NADPH metabolism, malic enzyme, encoded by *Men-b*, revealed greater variation across tissues, with fat body, glia, germline, and nervous system showing greater flux ranges **(Supplementary fig. 3g)**. Altogether, flux balance, coefficient of variation, and

variability analyses provide a quantitative evaluation of individual reaction rates across tissues, and the results point to enzymes that might underly key differences in specific pathways in different tissues.

Furthermore, rather than focusing on single enzymes, we estimated pathway flux using the pathway flux variability, which aggregates the range of individual reaction rates within a pathway multiplied by the pathway's total number of reactions. As expected, the analysis revealed a wide distribution of pathway flux variability across tissues **(Fig. 3b)**. For instance, fatty acid oxidation was predicted to have higher pathway flux variability in the fat body, oenocytes, and germline cells **(supplementary fig. 3h)**. Further, for the protein degradation pathway, muscle cells showed higher flux variability, an observation that agrees with the established function of muscle as a major site of amino acid breakdown. Moreover, pathways that share common intermediates exhibit similar patterns of pathway variability, confirming established interconnections among key metabolic pathways, e.g., glycolysis-pentose phosphate pathways, TCA cycle-oxidative phosphorylation pathways, and purine-pyrimidine pathways **(Fig. 3c-e and supplementary fig. 3i)**. Notably, fat body, oenocytes, and germline cells showed higher pathway flux variability in tyrosine, glycolysis, pentose phosphate pathway, BCAA and glutathione metabolism as compared to other tissues **(Fig. 3c)**. Additionally, polar follicle cells and multidendritic neurons were predicted to have lower pathway flux throughout the TCA, pyruvate, and oxidative phosphorylation pathways **(Fig. 3d)**. Follicle cells and germline cells also showed higher pathway flux in arginine and proline pathways, which might be relevant to a previous report that arginine influences egg laying capacity[47] **(Fig. 3e)**. Furthermore, based on the pathway flux variability analysis, we were able to identify 12 distinct tissue groups, demonstrating the similarities and differences across tissues **(Fig 3f).** Altogether, our results predict what enzymes have highly variable fluxes in different tissues and what pathways are variable across tissues, highlighting tissue-dependent metabolic pathway similarities and differences.

Metabolite profiling supports tissue-specific pathway analyses

To test the model-based prediction on tissue-specific metabolic pathway analysis, we performed metabolite profiling of approximately 300 polar metabolites across *Drosophila*'s head, thorax, gut, and abdomen, assessing their enriched metabolites and related pathways **(Fig. 4a)**. The head, thorax, and abdominal carcass are predominantly made up of CNS tissues, muscle, and the fat body plus oenocytes, respectively, and can be dissected relatively rapidly, minimizing perturbation of metabolites. Thus, we chose to focus on these three body regions, as well as the gut together with Malpighian tubules (MTs), kidney-like organs that are connected to the gut. Principal component analysis revealed distinct

metabolite profiles unique to each dissected body region **(Fig. 4b and supplementary Fig. 4a)**. Specifically, metabolites such as adenosine, adenylosuccinate, adenine, and AMP were highly enriched in thoraces compared to other regions **(Fig. 4c and supplementary Fig. 4b)**. These metabolites are often enriched in energy demanding tissues such as muscle, suggesting that these metabolites came from muscle in the thorax[4]. In heads, 4-aminobutyrate (GABA), N-acetyl-L-aspartate, GMP, and ascorbates were highly enriched **(Fig. 4d and supplementary Fig. 4c)**. GABA serves as an inhibitor of neurotransmitters and N-acetyl-L-aspartate is one of the amino acids highly enriched in the nervous system. In the gut plus MT samples, pyridoxine, betaine, uric acids, and S-ribosyl-L-homocysteine were highly enriched **(Fig. 4e and supplementary Fig. 4d)**. Pyridoxin (vitamin B6) and betaine are generally obtained from the food, which is consistent with the presence of these metabolites mainly in the gut[48,49]. Further, uric acids, which are mainly processed in MTs, were also present in our gut plus MT samples. In the abdominal carcass, we observed enrichment in nucleotide-related metabolites such as xanthosine and hypoxanthine, and in methionine-related metabolites such as methionine s-adenosyl-l-methioninamine and 5-methyl-THF **(Fig. 4f and supplementary Fig. 4e)**. We surmise that enrichment of these metabolites in the abdominal carcass reflect contributions of the fat body and oenocytes, which are known to be the major sites of de novo nucleotide synthesis[50].

Next, we performed a metabolite set enrichment analysis to determine which metabolic pathways were associated with what sets of enriched metabolites[51], and compared these results with our pathway flux analysis. The enrichment analysis revealed that highly enriched metabolites found in thorax muscle were involved in purine metabolism (KEGG id: dme00230) **(Supplementary Fig. 4f)**. This was consistent with our model-based pathway analysis results, in which we also found that muscle cells showed greater pathway flux variability in purine metabolism as compared to other pathways and across tissues **(Supplementary Fig. 4g)**. In heads, the enrichment analysis revealed that highly enriched metabolites were involved in alanine, aspartate, and glutamine metabolism (KEGG id: dme00250) **(Supplementary Fig. 4h)**. This was also consistent with our model-based analysis, in which many types of neurons showed greater pathway flux variability in this pathway compared to other pathways and tissues **(Supplementary Fig. 4i)**. Regarding the gut, the enrichment analysis revealed that enrichment of sets of metabolites were involved in pyrimidine metabolism, supporting the model-based prediction that enteroendocrine cells showed greater pathway flux variability in this pathway **(Supplementary Fig. 4j)**. In the abdominal carcass, the enrichment analysis revealed highly enriched set of metabolites were associated with nicotinate and nicotinamide metabolism (KEGG id: dme00760), and our model confirmed that tissues such as escort cell and follicle cells were predicted to have higher pathway flux variability in the pathway **(Supplementary Fig. 4k)**. Altogether, our body region-based metabolite profiling results revealed enriched sets of metabolites and their associated pathways, aligning with established metabolic

signatures of specific tissues and providing empirical support for predictions made by our tissue-specific metabolic pathway analyses.

^{13}C-isotope tracing and flux analysis identify GADPH as a rate-limiting enzyme in muscle under high sugar diet conditions

To test the utility of our tissue-specific GEMs in studies relevant to human metabolic diseases, we applied the muscle-GEM to investigate the effects of high sugar diet (HSD) on muscle metabolism. Chronic HSD has been shown to induce a type 2 diabetes-like syndrome in *Drosophila*[7] and decrease glucose utilization in leg muscle in type 2 diabetes patients[52]. To determine how glucose metabolism is altered in fly muscle in response to HSD, we fed w^{1118} male flies with high sugar diet that included uniformly labeled ^{13}C-glucose isotopic tracers **(Fig. 5a)**. The isotopic labeling patterns revealed a decrease in the contribution of glucose to glycolytic and TCA cycle intermediates. Specifically, the fractional enrichment of lower part of glycolytic intermediates was significantly reduced compared to the upper part of glycolytic intermediates **(Fig. 5b-d)**. Specifically, the fractional labeling of 1,3-bisphosphoglyceric acid (1,3-BPG), the product of glyceraldehyde 3-phosphate dehydrogenase (GAPDH), was nearly 90 % lower under HSD conditions. Additionally, we observed increased levels of upper glycolytic intermediates under HSD, including glyceraldehyde 3-phosphate, the substrate of GAPDH, having nearly 25 % higher (p-val = 0.02) **(Supplementary Fig. 5a)**. These suggested that accumulation of upper glycolytic intermediates was partly due to the decreased GADPH reaction rate, as shown from the isotopic labeling pattern. Furthermore, the fractional labeling of TCA cycle intermediates was more than 40 % lower in HSD conditions, with fumarate decreasing most significantly **(Fig. 5e-g)**. Altogether, these results indicated that glucose contribution to muscle was significantly lower under HSD condition, with GADPH potentially serving as a bottleneck reaction step in glycolysis.

Next, using ^{13}C-labeling patterns and the experimentally measured glucose uptake rates as constraints to the muscle-specific GEM, we performed flux balance, variability, and sampling analyses (see Methods) **(Fig 5h and supplementary fig 5b)**. The flux analyses predicted decreased rates in glycolysis, parts of the TCA cycle, and mitochondrial transport reactions **(Fig. 5i)**. Additionally, the model simulation demonstrated that the reaction rates in glycolysis were sensitive to changes in the glucose uptake and GADPH reaction **(supplementary fig 5c-d)**. Specifically, we performed a perturbation effect analysis, which is analogous to a sensitivity analysis, to determine how the changes in individual reaction rates influenced the overall glycolysis rate. Under HSD, the analysis revealed that a decrease in the GAPDH reaction rate influenced the summed glycolytic reaction rates most significantly,

suggesting the potential role of GAPDH as a rate-controlling enzyme **(Fig. 5j and supplementary fig. 5e).**

As GADPH requires NAD^+ as an electron acceptor, we wondered whether HSD increased the $NADH/NAD^+$ ratio, which could thermodynamically inhibit the GAPDH reaction **(Fig. 5k)**. Indeed, we observed that cellular $NADH/NAD^+$ ratio increased from 0.46 to 1.57 in response to HSD **(Fig. 5l)**. The total NADH and NAD^+ levels were also decreased in response to HSD, suggesting that HSD might influence *de novo* NAD^+ synthesis pathway **(Supplementary Fig. 5f)**. Next, to evaluate the potential source of increased $NADH/NAD^+$ that may inhibit GAPDH reaction, we evaluated NADH-dependent reaction rates from our flux sampling analysis. The model simulation predicted increased flux in aldehyde dehydrogenase reactions (*Aldh-III*, *T3dh*) **(Supplementary Fig. 5g)**. Moreover, it predicted a decreased flux in lactate dehydrogenase (LDH), a major site of NAD^+ regeneration **(Fig. 5m)**. Given the decreased NAD^+ regeneration from LDH, we wondered how NAD^+ was regenerated. We investigated NAD^+ regenerating enzymes and found out that the rate of glycerol-3-phosphate dehydrogenase 1 (GPDH1) was predicted to increase, potentially compensating for the reduced LDH reaction regenerating NAD^+ (**Fig. 5n and supplementary Fig. 5h**). Indeed, the contribution of NAD^+ regeneration from GPDH1 was predicted to increase from 4 % to 40 % in response to HSD (**Fig. 5o)**. Additionally, we found that the fractional enrichment of M+3 G3P increased by nearly 6-fold when compared to lactate, suggesting that the glucose contribution to G3P was greater than lactate in response to HSD (**Fig. 5p and q**).

Furthermore, as GAPDH contains reactive cysteine residues that can be oxidized, decreasing its reaction activity[53], we measured the oxidation state of GAPDH in thoracic muscles using a switch-tag redox proteomics approach (see Methods)[54]. In *Drosophila*, two isoforms of GAPDH are present, which are both closely related to the sequence of human GAPDH and known to serve partially redundant functions **(Supplementary Fig. 5i)**[55]. Although both GAPDH1/2 protein levels were not significantly changed, we found a statistically significant increase in oxidation at Cys-130, Met-127, 141 and 172 in GAPDH2, and at Met-40 in GAPDH1 (referenced to Uniprot:M9PJN8 for GAPDH2 and P07486 for GAPDH1) **(Supplementary Fig. 5j and k**). Additionally, we used AlphaFold to find out that Met-40 was positioned near NAD^+ binding site **(Supplementary Fig. 5l)**. The oxidation of this residue might interfere NAD^+ binding, contributing to alteration of GAPDH activity in *Drosophila* **(Supplementary Fig. 5m)**. Altogether, our results demonstrate the utility of applying our tissue-specific GEMs to quantitatively assess muscle metabolism in response to HSD, identifying GAPDH as a rate-limiting enzyme step and pointing to specific enzymes that may contribute to alteration of $NADH/NAD^+$ redox states.

Pathway flux index analysis identifies altered fructose and butanoate metabolism in muscle under HSD

To investigate what other metabolic pathways were altered in muscle under HSD, we introduced pathway flux index (PFI), which can estimate metabolic pathway activities by integrating the pathway flux variability with the mean reaction rates derived from sampling analysis (see Methods) **(Fig. 6a)**. Nearly 60% of the metabolic pathways showed a decreased PFI in response to HSD relative to NSD. Specifically, metabolic pathways such as glycolysis, oxidative phosphorylation, and the TCA cycle showed lower PFIs under HSD, aligning with our earlier observations **(Fig. 6b)**. These predictions were also supported by our redox proteomics analysis, in which we found commonly known rate-controlling enzymes in glycolysis, such as Pfk and Pyk, to be highly oxidized at their cysteine residues **(Supplementary fig. 6a).** A larger number of mitochondrial enzymes were also oxidized, including Kdn and Idh3, key enzymes that regulate TCA cycle **(Supplementary fig. 6b and c)**. Additionally, fructose metabolism revealed significantly reduced relative PFI, with the rate of fructose conversion to fructose-6-phosphate predicted to decrease by nearly 100-fold **(Fig. 6c).** In contrast, butanoate metabolism showed higher PFI than other pathways, with the rate of 3-hydroxybutyrate dehydrogenase predicted to increase by nearly 20-fold **(Fig. 6d).**

To test the results of PFI analysis, we conducted targeted metabolomics in thoracic muscles in response to HSD **(Fig. 6e)**. As expected, we found significant changes in metabolite pools under HSD compared to NSD, including metabolites found in fructose and butanoate metabolism **(Fig. 6f and supplementary fig. 6d)**. Related to fructose metabolism, we observed increased levels of sucrose/trehalose, sorbitol, and the upper part of glycolytic intermediates **(Fig. 6g and supplementary fig. 6e)**. Given the decreased glucose contribution to glycolysis and the reduced cellular level of ATP, which is required for the hexokinase reaction, the increased level of sorbitol suggested that carbon sources might be used for sorbitol production **(Supplementary fig. 6f)**. In butanoate metabolism, we found increased levels of acetoacetate and succinyl-CoA, and decreased levels of acetoacetyl-CoA and succinate, the substrates and products of the SCOT enzyme, respectively **(Fig. 6h and supplementary fig. 6g)**. The ratio between the products and substrates decreased by nearly 7-fold, indicating a potential thermodynamic shift in conversion of acetoacetate to acetoacetyl-CoA **(Supplementary fig. 6h)**. This directionality is consistent with the predicted rate of conversion of 3-hydroxybuyrate to acetoacetate, which is subsequently oxidized to actoacetyl-CoA. Altogether, our pathway flux index analysis demonstrated its application in further exploring and identifying additionally perturbed metabolic pathways in muscle in response to HSD.

Discussion

Drosophila serves as a powerful model for the study of human metabolic diseases, which would be enhanced by the availability of computational tools for quantitative assessment of tissue-specific metabolic networks and pathway activities. To fill this gap, we generated tissue-specific GEMs for adult *Drosophila* tissues using pseudo-bulk single-cell RNA sequencing. The results of our metabolic network analysis not only recapitulated known metabolic functions of individual tissues, but also revealed distinct metabolic network structures across tissues. This information is valuable as currently available GEMs for *Drosophila*, such as Fruitfly1[25], FlySilico[23], and iDrosophila[24], are not tissue-specific, used for larvae, or used for a specific brain disease model, respectively. Furthermore, while previous GEMs in *Drosophila* did not consider enzyme constraints, we integrated enzyme kinetics and abundances into each tissue-specific GEM, revealing maximum rate distributions across tissues. Additionally, as the available GEMs for *Drosophila* generally focused on reconstruction of a core metabolic network, they provide limited information about fluxes in various metabolic pathways. In this regard, our flux analyses on the tissue-specific GEMs provide quantitative information that improves metabolic phenotype predictions of individual tissues.

Moreover, we demonstrated the effectiveness of applying tissue-specific GEMs to identify metabolic vulnerabilities in disease states, such as the effect of HSD on muscle metabolism. To improve our GEM-based model prediction, we also incorporated ^{13}C-glucose isotopic tracing experimental data as constraints to the central carbon metabolism activities in our muscle-specific GEM[56,57]. Through the integrated analysis, we identified GAPDH as a rate-limiting reaction step in glycolysis in muscle in response to HSD. Particularly, our model-based simulation predicted that NADH/NAD$^+$ imbalance was caused by the altered aldehyde and lactate dehydrogenase reaction rates, contributing to the inhibition of the GAPDH reaction. While the oxidation of GAPDH was shown to alter glycolytic activity[58], our data indicates that both NADH/NAD$^+$ imbalance and GAPDH oxidation state may contribute to the inhibition of GAPDH reaction rates in muscle in response to HSD.

Beyond glucose metabolism, we further demonstrated the power of GEM-based analysis to identify other dysregulated pathways in muscle under HSD. As metabolism is highly flexible, it is generally not a single metabolite, enzyme, or pathway that regulates tissue homeostasis[59]. Thus, identifying other perturbed metabolic pathways is critical for studying disease-related changes in metabolism. Our pathway flux index, which is an extension of flux balance analysis, provided potential candidates. Through both computational and experimental approach, we not only confirmed previously known perturbed metabolic pathways associated with type 2 diabetes muscle in humans, but also revealed

that fructose and butanoate metabolism were perturbed in muscle in response to HSD. In particular, the increased sorbitol level suggests that the decreased fructose metabolism might shift its reaction toward production of sorbitol, rather than being catabolized by glycolysis. Indeed, as the sorbitol metabolism is dependent on NAD(P)H redox states, the perturbed $NADH/NAD^+$ redox state could inhibit the sorbitol dehydrogenase reaction, contributing to the accumulation in muscle. While activation of sorbitol production pathways has been reported in diabetic liver[60], our results suggest that this pathway might also serve as a metabolic signature in type 2 diabetes muscle. Furthermore, our model also predicted an increased reaction rate of BDH1 in butanoate metabolism. While *Drosophila* glia were shown to synthesize ketone bodies to fuel neurons during starvation[61], our model predicted that ketone bodies might be used as alternative fuel in muscle in response to HSD. Indeed, in type 2 diabetic mouse model, the inhibition of ketone body oxidation in muscle by knocking down succinyl CoA:3-ketoacid CoA transferase (SCOT) was shown to alleviate hyperglycemia[62]. Altogether, our GEM-based flux analyses demonstrated its utility in identifying both key enzymes and the perturbed pathways that characterized muscle metabolism in response to HSD.

Finally, we note that our reconstructed tissue-specific metabolic models can be adapted for studying other human metabolic diseases. For example, cancer cachexia is a systemic wasting syndrome caused during cancer development that leads to weight loss and dysregulated metabolism in peripheral tissues such as muscle and adipose tissues[63]. Several cancer cachexia models are available for *Drosophila*[9] and our tissue-specific GEMs will be useful to interrogate tumor and host metabolism. Additionally, in the future, tissue-specific GEMs can be integrated with spatial isotope tracing analysis. Mass-spectrometry based imaging analysis enables quantification of pathway activities at spatial resolution.[64] Integration of these datasets into tissue-specific GEMs should enhance our understanding of tissue-specific metabolism. Thus, our reconstruction of tissue-specific GEMs in *Drosophila* and subsequent flux analyses represents a significant advance in quantitative assessment of tissue-specific metabolism and highlights the usefulness of these applications to identify perturbed metabolic processes in disease states.

Methods

Contextualization of genome-scale metabolic model

Update on genes and gene-transcript-protein-reaction associations

Fruitfly1.0 is a generic metabolic model describing metabolic networks of *Drosophila melanogaster*[25]. To update the gene information, we used Gene List Annotation for Drosophila (GLAD) database that contained a metabolic gene set of 2,629 genes (https://www.flyrnai.org/tools/glad/web/, Metabolic_vs3, data attached) and compared them with the genes listed in the GEM. We found out that 1,465 genes from GLAD were not included in the GEM. These missing genes from Fruitfly1 included genes considered as transcription factors, kinases, phosphatases, and dehydrogenases. Instead of manually checking all the genes and link the information to the GEM, we focused on fly genes whose orthologs are present in human and for which the reaction information, including the associated substrates and products, are already present in the human-GEM. Since the human-GEM and Fruitfly1 share reaction and metabolites annotations[65], we added the genes and related information to Fruitfly1. To avoid introducing noise at ortholog mapping step, we focused on genes that were highly conserved. Of 1,465 genes analyzed, 564 genes (38.5 %) were predicted to have human orthologs assigned with high rank based on DIOPT score[66]. Of these, 36 genes were linked to reactions and gene-rules in human-GEM. We added these genes into Fruitfly1 (see Supplementary Data). For reactions that already had the grRules, we added new genes to the existing rule with 'or'. To exclude the redundant genes present in the gene list in Fruitfly1, we also investigated the redundancies and found out that three gene symbols (*Sur/sur, Argk2/CG5144, and Argk/Argk1*) were mapped to the same FlyBase gene IDs. To remove the redundancies, we only used *Sur* (FBgn0028675)*, Argk2* (FBgn0035957)*, Argk1* (FBgn0000116). Altogether, we named this GEM as Fruitfly2.

Update the Enzyme Commission number to Fruitfly2

To integrate the kinetics data to the reaction, it is useful to link reaction information with Enzyme Commission (EC) numbers. Fruitfly2 already contained some reactions linked to EC numbers. As we investigated the reactions missing with EC numbers, we found that 7411 out of 12038 reactions were not associated with EC numbers. We evaluated whether these reactions had an associated KEGG reaction ID, such that we could use the KEGG reaction IDs to link the reactions to the EC numbers. We found that only 151 reactions were linked to KEGG reaction IDs. Of these, 78 KEGG reaction IDs were linked to EC numbers. Using this information, we linked these 78 reactions to EC numbers. Next, rather than focusing on reactions, we investigated the genes that were linked to reactions. As genes were linked to

KEGG reaction IDs, we could use this information to link EC numbers to reactions. Through this analysis, we added 576 EC numbers to the reactions without EC numbers. Altogether, we added a total of 654 EC numbers to the reactions that were not previously linked to EC numbers in Fruitfly2 (see Supplementary Data). We named this GEM with updated EC numbers as Fruitfly3.

Generation of tissue-specific metabolic models using tINIT

Using an updated version of the tINIT (task-driven integrative network inference for tissues) algorithm[36,65], we reconstructed tissue-specific genome-scale metabolic models. The updated tINIT algorithm utilizes a mixed-integer linear programming approach to optimize the objective function. This optimization aims to include as many reactions as possible based on transcriptomic and/or proteomic evidence, while reducing the inclusion of reactions associated with enzymes that show low or no expression. Additionally, the algorithm ensures that every reaction in the final model carries fluxes, ensuring the model's connectivity. The final model requires to execute specific metabolic functions, such as biomass synthesis or ATP re-phosphorylation, which were predefined as an input of a list of 57 metabolic tasks. The updated version of tINIT algorithm, *getINITModel2* function on the Human-GEM GitHub repository, differentiates the isoenzymes and complex subunits. For tissue-specific transcriptomics data, we generated pseudo-bulk RNA seq data for 32 different tissues from the snRNA-seq database from Fly Cell Atlas as input for the tINIT algorithm. As most of the tissues showed the averaged gene expression levels around one, we used a value of one as a gene expression threshold, keeping the same constraint applied to all models.

Metabolic network structure, subsystem coverage, and functional analysis

The analysis was followed based on previously reported protocol[65]. In brief, to compare model structures, we used *compareMultipleModels* function from the RAVEN package, in which a binary reaction matrix is formulated with rows and columns representing reactions and the GEMs, respectively. A value of one indicated the presence of a reaction in a GEM, while zero denoted its absence. The t-distributed stochastic neighbor embedding (tSNE) on the binary reaction matrix was used to visually compare GEM reaction content in two dimensions, using the Hamming distance as the distance metric. The results were also presented as a clustered heatmap, with colors indicating the degree of Hamming similarity.

Variation in model structures were further investigated by analyzing the coverage of metabolic subsystems in the GEMs. Subsystem coverage (SC) refers to the number of reactions that are present to a

specific metabolic subsystem. The coverage of each metabolic pathways was computed and compared to the average coverage across all the tissue-specific metabolic models. The deviation of a subsystem coverage from the mean coverage was calculated as a percentage for each subsystem as follows:

$$\%\ differences\ in\ subsystem\ coverage = \frac{SC - SC_{mean}}{SC_{mean}} \times 100\ \%$$

To facilitate the visualization of subsystem coverage, we set the threshold of 100 % to show only the metabolic pathways in which at least one tissue has more than 100 % differences compared to the mean.

For assessment of metabolic functionality of individual tissues, the ability of each GEM to perform a predefined set of 256 metabolic tasks was evaluated[65,67]. The RAVEN's *checkTasks* function was utilized for task assessment, with a task considered failed if the model could not execute the defined function, and passed if it could. Subsequently, we counted the number of tasks completed by each tissue-GEM and the values were compared using z-score. The results were represented as heatmaps.

Protein abundance calculation

Protein abundance estimation from mRNA levels

This method determines the protein abundance based on gene expression dataset by applying the translational and degradation rate parameters and evaluate whether the pipeline is valid. The general pipeline was adapted from published protocols[42,43]. The protein abundance can be calculated by solving a differential equation in which the change in protein level is a function of the translation rate of mRNAs, the amount of mRNAs, and the degradation rate of proteins. Assuming a steady-state approximation, protein levels can be directly calculated given mRNAs level and the translation and degradation rates are known. Although Schwanhausser et al. determined the kinetic parameters from mammalian tissue cultures and mouse cell lines, the values were within the order of magnitude different across organisms including Drosophila[68,69]. Thus, we used these values to calculate the protein abundance from mRNA levels.

Next, we downloaded from FlyBase (release 2022_05) gene expression datasets based on bulk RNA-seq experiments from dissected tissues, covering 17,750 genes and the corresponding reads per kilobase per million reads (RPKM). Since the proteome dataset from PaxDb is based on the integrated dataset, we averaged the gene values across 11 different datasets that represented the RNA levels of the whole adult organism, while excluding larvae and embryo datasets. RPKM values were converted to mRNA copy numbers using the following equation:

$$\text{mRNA copy numbers} = RPKM * \frac{1}{10^9} * \mathrm{T} * \mathrm{N_A}$$

, where

N_A is the Avogadro's number

T is the mRNA nucleotides per cell.

$N_A = 6.022 \times 10^{23}$ and $T = 2.6 \times 10^{-15}$ were used. The rate of change of protein level can be expressed as a function of translation rate of mRNA level and degradation rate of protein level.

$$\frac{d[Protein]}{dt} = k_{trans}[mRNA] - k_{degra}[Protein]$$

Assuming steady state approximation, we can simplify the equation to

$$Protein = mRNA * \frac{k_{trans}}{k_{degra}}$$

To convert protein copy numbers to parts per million, we used the following equation:

$$\text{protein parts per million} = \frac{\mathrm{P} * \mathrm{L}_{ss} * M_w}{N_A * m_T} * 10^3 ,$$

where

P: Protein copies per cell

$\mathrm{L_{ss}}$: Amino acids length per protein

$\mathrm{M_w}$: Average mass per amino acid

$\mathrm{N_A}$: Avogadro's number

m_T: Total mass of protein per cell

$\mathrm{M_w} = 110$ and $\mathrm{m_{tot}} = 150 \times 10^{-12}$ were used[70].

PaxDb proteome comparison analysis

This method compares the predicted enzyme abundance with the experimentally measured enzyme levels. We downloaded from Protein Abundances Across Organisms database (PaxDb, pax-db.org)[71] the experimentally measured protein levels, covering 13,264 proteins in the whole organism. We compared these datasets to our predicted enzyme levels.

Acquisition of turnover number

Enzyme turnover numbers for *Drosophila melanogaster, Homo sapiens, Mus musculus, C. elegans,* and *Danio Rerio* were downloaded through BRENDA API (see supplementary data)[44]. For multiple values reported from the same unique EC numbers, we used the highest value because the purpose of this analysis was to calculate the maximum velocity. For simplicity, we also did not consider the effect of temperature and pH values on kcat values. For *Drosophila,* we identified 39 unique enzyme commission numbers **(Supplementary Fig. 2f and g**). As the turnover numbers of *Drosophila* were also limited, we evaluated the order of magnitudes of kcat values across other organisms and filled the missing kcat values using those values from other organisms given that the corresponding kcat values were within one order of magnitude **(Supplementary Fig. 2h**). Additionally, because BRENDA did not have all the kcat values for unique EC numbers, we loosened the constraints such that enzymes that were associated with EC numbers in Fruitfly3 could have kcat values, an approach adopted from Lewis *et al.*[42]. For instance, if the turnover data for enzyme with EC: 1.1.1.49 was not available, we used the highest kcat values from enzymes with EC:1.1.1.x. Although loosening the constraints might not precisely present the kcat values of uncharacterized enzymes, we found this approach reasonable as the EC numbers with less digits present a progressively loosened classification of the enzyme.

Gene ontology enrichment analysis

To evaluate the biological processes that were highly enriched for calculated maximum reaction rates, we used the *enrichGO* function from clusterProfiler package and FlyBase identifiers. Results were visualized through dot plots. Hypergeometric distribution was used to calculate the adjusted p-values.

Flux balance analysis

Flux balance analysis was performed to determine the optimal metabolic flux distributions that maximizes the objective function, while satisfying the stoichiometric constraints under steady state assumption[17]. A metabolic network can be reconstructed by a stoichiometric matrix S of size m × n, in which m and n represents the number of metabolites and reactions, respectively, within the give network. The elements in S_{ij} equals to the stoichiometric coefficient of the metabolites i in reaction j. The relationship between metabolite and reaction rates can be represented as follows:

$$S\mathbf{v} = \frac{d\mathbf{m}}{dt}$$

, where **v** is the v by 1 vector of reaction rate vector and **m** is the m by 1 vector of metabolite concentrations. For flux balance analysis, we assumed the metabolic steady state and the change of concentration over time does not change, making the right side equal to 0. The flux balance analysis is to solve the optimization problem in which the objective function is represented by linear relationship and the constraints are formulated as follows:

$$\text{maximize } \mathbf{c}^T\mathbf{v},$$

$$\text{subject to } S\mathbf{v} = 0,$$

$$\text{and } \mathbf{v_{min}} \leq \mathbf{v} \leq \mathbf{v}_{max}$$

, where

S : Stoichiometry matrix with m metabolites and n reactions

c : vetor describing the linear objective function

v : decision variables that represent rates at steady state, or fluxes

$v \in R^n$

v_{min}, v_{max}: minimum and maximum fluxes

Objective function

ATP is an essential cofactor that provides energy to maintain and support a variety of metabolic processes, while NADPH is an ultimate reducing cofactor that serves as an electron donor for antioxidant defense and lipid synthesis[72]. NAD^+ is an electron acceptor and cells maintain higher NAD^+ to ensure metabolic processes such as glycolysis are working normally[73]. Based on these reasons and their commonality across the tissues, we generated the following three demand functions that are essential for cell survival:

$$\text{ATP maintenance function } (v_{\rightarrow ATP}): \text{atp [c]} + \text{atp [m]} + H_2O\text{ [c]} + H_2O\text{ [m]} \rightarrow \text{adp [c]} + \text{adp [m]} + H^+\text{ [c]} + H^+\text{ [m]} + P_i\text{ [c]} + P_i\text{ [m]}$$

$$\text{NAD demand function } (v_{\rightarrow NAD^+}): NAD^+\text{ [c]} + H^+\text{[c]} + NAD^+\text{ [m]} + H^+\text{[m]} \rightarrow \text{NADH [c]} + \text{NADH [m]}$$

NADPH demand function ($v_{\rightarrow \boldsymbol{NADPH}}$): $NADP^+$ [c] + H^+[c] + $NADP^+$ [m] + H^+[m] → NADPH [c] + NADPH [m]

The objective function with $\mathbf{c}^T$ of 1/3 is defined as

$$z_{common} = \mathbf{c}^T(v_{\rightarrow ATP} + v_{\rightarrow NAD^+} + v_{\rightarrow NADPH})$$

^{13}C-labeling pattern as constraints

As ^{13}C-labeling patterns indirectly provide information on pathway flux[74], we used the labeling pattern as the constraints to the GEM. First, we defined alpha, which is the ratio between the fractional enrichment of M+2 metabolites from [U-^{13}C]glucose under two different conditions. In our case, we used the ratio between high and normal sugar diet conditions. Next, as the extent of labeling of M+2 metabolites partly reflect the pathway activity in glycolysis and TCA cycle, these ratios can be approximated as the relative change of the reaction rates that produced these M+2 metabolites, and could be represented as follows:

$$\alpha = \frac{FE_{M+2_{HSD}}}{FE_{M+2_{NSD}}} \cong \frac{r_{HSD}}{r_{NSD}}$$

Next, we used this relative ratio as the constraint to upper limit reaction rates under HSD:

$$v \leq \alpha \times v_{max}$$

For simplicity, we also applied this constraint to the lower limit reaction rates (v_{min}) for reversible reactions.

Flux variability analysis

Flux variability analysis (FVA) provides the range of fluxes obtained when the objective functions are sub-optimal conditions[46]. FVA solves two optimization problems for each v_i of interest,

$$\text{maximize / minimize } v_i,$$

$$\text{subject to } S\mathbf{v} = 0,$$

$$\mathbf{c}^T\mathbf{v} \geq \alpha \times z_{common,opt},$$

$$\text{and } \mathbf{v_{min}} \leq \mathbf{v} \leq \mathbf{v}_{\boldsymbol{max}}$$

, where

α : optimality paramter $(0 \leq \alpha \leq 1)$, where 1 is equal to optimal condition

$z_{common,opt}$: Optimal solution obtained from flux balance analysis

The results of the analysis provide the maximum and minimum flux values of individual reactions.

Flux sampling analysis

We replaced the unconstrained flux ranges to the minimum and maximum flux values obtained from the flux variability analysis. The random sampling of the solution space was determined using GpSampler algorithm, which implemented the Artificial Centering Hit-and-Run algorithm[75]. A total of 10,000 random sample points was used as initial input points for sampling.

Perturbation effect analysis

We conducted a computational perturbation effect analysis which quantifies the impact of individual enzyme perturbations on the reaction rates of other enzymes in glycolysis. The maximum rates of individual reactions were reduced by 10 % and the flux variability analysis was performed. The mean rate of individual reaction rates in glycolysis were calculated by averaging the minimum and maximum rates allowed in individual reaction steps. The perturbation effect was defined by the summed reactions rates in glycolysis, normalized to the change of maximum reaction rates of perturbed enzyme rate.

Definition of pathway flux variability and pathway flux index

Quantification of fluxes through metabolic pathways provides a better insight into metabolic phenotypes, as the set of metabolic processes, rather than a single enzyme, provide metabolic precursors that are essential for cell survival and proliferation[2]. We defined the pathway flux variability as follows:

$$pathway\ flux\ variability = n \sum_{i=1}^{n} (v_{i,max} - v_{i,min})$$

,where

v: reaction rates obtained from flux variability analysis

n: reaction number in the pathway

Essentially, the pathway flux variability is the summed reaction ranges in a pathway, weighted by the total number of reactions. We multiplied the range to the total number of reactions to give the weight that pathways having more reaction contents are likely to carry more flux within the pathway.

While pathway flux variability provides the range of fluxes in a defined pathway, it does not provide the information of the expected flux values of individual reactions. To resolve this issue, we defined pathway flux index as follows:

$$pathway\ flux\ index = n \sum_{i=1}^{n} \mu_i \times (v_{i,max} - v_{i,min})$$

,where

μ_i: the mean reaction rates obtained from flux sampling analysis

Fly stocks and maintenance

All flies were reared at 25°C and 60% humidity with a 12-hour on/off light cycle on standard laboratory food. Standard laboratory food is made as follows: 12.7 g/liter deactivated yeast, 7.3 g/liter soy flour, 53.5 g/liter cornmeal, 0.4% agar, 4.2 g/liter malt, 5.6% corn syrup, 0.3% propionic acid, and 1% Tegosept/ethanol. The semi-defined synthetic media for high sugar and normal diet were made according to the previously reported recipe[11], with a slight modification of sugar concentration. The normal diet (NSD) consisted of 10 g/L of agar, 80 g/L of yeast, 20 g/L of yeast extract, 20 g/L of peptone, 262 mM of sucrose, 0.3% propionic acid, and 1% Tegosept/ethanol. The high sugar diet (HSD) consisted of the same amount of all the components except 1 M of sucrose. For diet intervention experiments, we collected 2 – 4 days old w^{1118} male flies and transferred approximately 30 flies to vials containing either NSD or HSD. The food was replaced every two days.

Intracellular metabolites extraction and LC/MS analysis

Metabolites quantification in *Drosophila* were adapted from a published protocol[33,35]. 20 thoraces, head, gut, and abdomen were dissected in ice-cold 0.9% normal saline buffer after placing the flies under light CO2 anesthesia. Dissected thoraces were immediately placed in 1.5 mL tubes in dry ice. 450 µL of cold 80% (v/v) aqueous methanol were added to the tubes, and intracellular metabolites were extracted by

homogenizing tissues with pellet pestle for 1 minute by repeating a cycle of 20 seconds of grinding and 10 seconds of break. Samples were centrifuged at maximum speed for 10 minutes in the cold room. Supernatants were transferred to a new 1.5 mL tube, pelleted by vacuum centrifugation using speedvac and stored in -80 °C until mass-spectrometry analysis.

Samples were re-suspended using 22 uL HPLC grade water for mass spectrometry. 5-7 µL were injected and analyzed using a hybrid 6500 QTRAP triple quadrupole mass spectrometer (AB/SCIEX) coupled to a Prominence UFLC HPLC system (Shimadzu) via selected reaction monitoring (SRM) of a total of 300 endogenous water soluble metabolites for steady-state analyses of samples. Some metabolites were targeted in both positive and negative ion mode for a total of 311 SRM transitions using positive/negative ion polarity switching. ESI voltage was +4950V in positive ion mode and –4500V in negative ion mode. The dwell time was 3 ms per SRM transition and the total cycle time was 1.55 seconds. Approximately 9-12 data points were acquired per detected metabolite. For targeted 13C flux analyses, isotopomers from ~140 polar molecules were targeted with a total of 460 SRM transitions. Samples were delivered to the mass spectrometer via hydrophilic interaction chromatography (HILIC) using a 4.6 mm i.d x 10 cm Amide XBridge column (Waters) at 400 µL/min. Gradients were run starting from 85% buffer B (HPLC grade acetonitrile) to 42% B from 0-5 minutes; 42% B to 0% B from 5-16minutes; 0% B was held from 16-24 minutes; 0% B to 85% B from 24-25 minutes; 85% B was held for 7 minutes to re-equilibrate the column. Buffer A was comprised of 20 mM ammonium hydroxide/20 mM ammonium acetate (pH=9.0) in 95:5 water:acetonitrile. Peak areas from the total ion current for each metabolite SRM transition were integrated using MultiQuant v3.2 software (AB/SCIEX).

Metabolites profiling data analysis

Statistical analysis was performed using MetaboAnalystR[51]. The hierarchical clustering analysis and heatmap was generated using *PlotHeatMap* function, in which *hclust* function used to normalize the data across the samples and the Euclidean distance and ward.d were used as parameters for clustering algorithm. Principal component analysis was performed using *PCA.anal* function and the partial least squares – discriminant analysis (PLS-DA) was performed using *PLSR.Anal* function. In comparison of the means of the normalized metabolite peaks, the anova test was used using *ggpubr* package in R. For evaluation of the normalized metabolites peak areas, the peak areas were normalized to the protein mass of individual tissues. Metabolites without detection were omitted for calculation of the average.

^{13}C-isotopic labeling experiments and mass isotopomer analysis

To keep the molar ratio of the labeled glucose to sucrose consistent, we prepared the normal and high sugar diet with 13 mM and 50 mM of [U-$^{13}C_6$]glucose, respectively. For ^{13}C-isotopic labeling experiments, we collected 2 – 4 days old w^{1118} male flies and placed approximately 30 flies in vials containing either NSD or HSD with isotope tracers at room temperature. The food was replaced every two days. On day five, twenty thoraces were dissected per biological replicate and intracellular metabolites were extracted using 80% (v/v) aqueous methanol. Q1/Q3 SRM transitions for incorporation of 13C-labeled metabolites were established for polar metabolite isotopomers, and data were acquired by LC-MS/MS. Peak areas were generated using MultiQuant version 2.1 software. The natural isotope abundance was corrected using AccuCor (Github: https://github.com/XiaoyangSu/AccuCor)[77].

Switch-tagging redox proteomics

Muscle tissues were solubilized in 4% SDS in 100mM triethylammonium bicarbonate (TEAB) pH 7.0 lysis buffer and digested using S-Trap micro columns (Protifi, Huntington, NY) following the manufacturer's procedure. Each sample was loaded onto individual Evotips for desalting and washing. The Evosep One system (Evosep, Odense, Denmark) was used to separate peptides on a Pepsep colum (150 um inter diameter, 15 cm) packed with ReproSil C18 1.9 um, 120A resin using pre-set 15 samples per day gradient. The system was coupled to the timsTOF Pro mass spectrometer (Bruker Daltonics, Bremen, Germany) via the nano-electrospray ion source (Captive Spray, Bruker Daltonics). Raw data files conversion to peak lists in the MGF format, downstream identification, validation, filtering and quantification were managed using FragPipe version 13.0. MSFragger version 3.0 was used for database searches against a Drosophila database with decoys and common contaminants added.

Prediction of Drosophila GAPDH Protein Complexes Using AlphaFold-Multimer

For the prediction of protein complexes using AlphaFold-Multimer (AFM), we employed LocalColabFold version 1.5.2[78]. It integrates AFM version 2.3.1[79] and utilizes MMseqs2 for generating multiple sequence alignments. Computations were performed on the Harvard O2 high-computing cluster. Our prediction involved five models for each complex, each undergoing five recycling iterations. The model displaying the highest prediction quality was selected for each protein complex. The protein

complexes examined in this study include Drosophila GAPDH1 homodimer, GAPDH1:GAPDH2 heterodimer, and GAPDH2 homodimer. The prediction results have been made publicly available on the Fly Predictome website (https://www.flyrnai.org/tools/fly_predictome/web/)[80]. For visualization of the predicted structures we utilized ChimeraX (PMID: 37774136).

ATP quantification

ATP quantification was adapted from a published protocol[81]. Three biological replicates, each with 4 thoraces were homogenized in 100 µl of 5 M guanidine-HCl (Sigma) supplemented with 100 mM Tris pH 8.0 and 5 mM EDTA pH 7.8, immediately boiled for 3min at 95 °C, and centrifuged at 15,700 g, at 4 °C, for 10 min to collect the supernatant. Extracts were used for quantification of luciferase as proxy for ATP content using the ENLITEN ATP Assay System Bioluminescence Detection Kit (Promega) according to the manufacturer instructions. Samples were diluted in water to fit the range of the standard curve (5 serial dilutions, 1:10). ATP levels were calculated from the standard curve by measuring luminescence (Relative Light Units) in a SpectraMax Paradigm Multi-mode microplate reader (Molecular Devices) using Corning 96-well Solid White Flat Bottom Polystyrene microplates (Costar). Values were normalized to protein content (Pierce BCA Protein Assay Kit).

Quantification of cellular NADH/NAD^+

Measurements of NADH/NAD^+ was adapted from a published protocol[82], using the NADPH/$NADP^+$ Glo Assay (Promega) with a modification in manufacturer instruction. In brief, five thoraces were dissected, weighted, and stored in 1.5 mL tubes in dry ice. 300 µL of PBS with 1 % DTAB solution was added the tubes and the thoraces were homogenized with the pellet and homogenizer. 110 µL of the cell lysates were split into two separate ice-cold 1.5 mL tubes: one for NADH and the other for NAD^+. For NAD^+ tube, 55 µL of 0.4 M HCl with 1 mM ascorbate were added. We added ascorbic acid to prevent the oxidation of NADH into NAD^+ under low pH, avoiding the overestimation of intracellular NAD^+ levels[83]. The other NADH tube remained untreated. Both tubes were placed into the heat block with 60 °C temperature for 20 minutes to destroy NAD^+. Tubes were equilibrated at room temperature for 10 minutes. 55 µL 0.5 M Trizma/base was added to the NAD^+ tubes to neutralize the acid, while 110 µL of HCl/ascorbate/base buffer was added to the untreated NADH tube. Afterwards, NADH, NAD^+, and the ratio were measured following the manufacturer's instruction with the generation of standard curves with known concentration.

Data analysis, statistics, and reproducibility

Statistical analyses were performed in GraphPad Prism (v9.5.1), MATLAB (2020b), or R (4.2.1). For analysis of two groups, Welch's unequal variances t-test was used to calculate a p-value. For multiple comparison, Bonferroni method was used for correction. The significance was represented as follows: $*$ $P < 0.05$, $**$ $P < 0.01$, $***$ $P < 0.001$,$****$ $P < 0.0001$. For analysis of more than two groups, one-way ANOVA was used to calculate a p-value in comparison of the metabolomics dataset across four different regions. For isotope tracing analysis, we applied the two-sample t-test, a parametric test that compares the location parameter of two independent data samples. For gene ontology analysis, we used the hypergeometric distribution to calculate p-values. No data was excluded from statistical analysis.

Data Availability

Source data, including raw data for ^{13}C-glucose isotope tracing experiment, HSD metabolomics, tissue metabolomics and redox proteomics, are provided with this paper.

Code Availability

MATLAB scripts used for genome-scale metabolic modeling and flux analyses are available on GitHub (https://github.com/sunjjmoon/FlyTissueGEMs).

Author Contributions:

Conceptualization, S.J.M. and N.P.; Methodology, S.J.M., M.D., A.R.K., J.A., P.C., and N.P.; Investigation: S.J.M., Y.H., M.D., A.R.K., P.C., J.A.; Writing – Original Draft, S.J.M.; Writing – Review and Editing, S.J.M., Y.H., M.D., A.R.K., P.C., J.A., A.D. and N.P.; Supervision, N.P.

Acknowledgements

We thank members of the Perrimon laboratory for useful discussions and experimental advice, including Dr. Stephanie Mohr for feedback on the manuscript. We also thank to the Research Computing Group at Harvard Medical School for access to the O2 High Performance Compute Cluster. We additionally thank Dr. Anush Chiappino-Pepe and Dr. Steven Marygold for valuable feedback on genome-scale metabolic modeling work. We also thank Dr. Jason Tennessen for valuable feedback on fly metabolism. We also thank Dr. Travis Nemkov for valuable feedback on metabolomics analysis. We also thank Dr. Safak Yilmaz and Dr. Marian Walhout for valuable feedback on genome-scale metabolic models. The mass spectrometry work was partially funded by NIH grants 5P01CA120964 (J.M.A.) and 5P30CA006516 (J.M.A.). This research was supported by NIH/NIDDK 1R01DK136945, NIH NIAMS R01 AR057352, Cancer 509 Research UK (CGCATF-2021/100022) and the National Cancer Institute (1OT2 CA278685-01). NP is an investigator of Howard Hughes Medical Institute. This article is subject to HHMI's Open Access to Publications policy. HHMI lab heads have previously granted a nonexclusive CC BY 4.0 license to the public and a sublicensable license to HHMI in their research articles. Pursuant to those licenses, the author-accepted manuscript of this article can be made freely available under a CC BY 4.0 license immediately upon publication.

Declaration of interests

The authors declare no competing interests.

References

1. Priest, C. & Tontonoz, P. Inter-organ cross-talk in metabolic syndrome. *Nat. Metab.* **1**, 1177–1188 (2019).

2. Metallo, C. M. & Vander Heiden, M. G. Understanding Metabolic Regulation and Its Influence on Cell Physiology. *Mol. Cell* **49**, 388–398 (2013).

3. Jang, C. & Sheng Hui, Xianfeng Zeng, Joseph H. Gorman III, Robert C. Gorman, J. D. R. Metabolite Exchange between Mammalian Organs Quantified in Pigs Resource. *Cell Metab.* **30**, 594-606.e3 (2019).

4. Chatterjee, N. & Perrimon, N. What fuels the fly: Energy metabolism in Drosophila and its application to the study of obesity and diabetes. *Sci. Adv.* **7**, 1–15 (2021).

5. Ugur, B., Chen, K. & Bellen, H. J. Drosophila tools and assays for the study of human diseases. *DMM Dis. Model. Mech.* **9**, 235–244 (2016).

6. Dam, E. Van, Santos, E., Franke, A., Kaleta, C. & Cocheme, H. M. Sugar-Induced Obesity and Insulin Resistance Are Uncoupled from Shortened Survival in Drosophila Article Sugar-Induced Obesity and Insulin Resistance Are Uncoupled from Shortened Survival in Drosophila. *Cell Metab.* 710–725 (2020) doi:10.1016/j.cmet.2020.02.016.

7. Musselman, L. P. *et al.* A high-sugar diet produces obesity and insulin resistance in wild-type Drosophila. *Dis. Model. Mech.* **849**, 842–849 (2011).

8. Parkhitko, A. A. *et al.* Downregulation of the tyrosine degradation pathway extends drosophila lifespan. *Elife* **9**, 1–27 (2020).

9. Kwon, Y. *et al.* Systemic Organ Wasting Induced by Localized Expression of the Secreted Insulin / IGF Antagonist ImpL2. *Dev. Cell* **33**, 36–46 (2015).

10. Hudry, B. *et al.* Sex Differences in Intestinal Carbohydrate Metabolism Promote Food Intake and Sperm Maturation. *Cell* **178**, 901-918.e16 (2019).

11. Tennessen, J. M., Barry, W. E., Cox, J. & Thummel, C. S. Methods for studying metabolism in Drosophila. *Methods* **68**, 105–115 (2014).

12. Heidarian, Y. *et al.* Metabolomic analysis of Drosophila melanogaster larvae lacking pyruvate kinase . *G3 Genes, Genomes, Genet.* **14**, 1–14 (2023).

13. Albrecht, S. C., Barata, A. G., Grobhans, J., Teleman, A. A. & Dick, T. P. In Vivo Mapping of Hydrogen Peroxide and Oxidized Glutathione Reveals Chemical and Regional Specificity of Redox Homeostasis. *cell Metab.* 819–829 (2011) doi:10.1016/j.cmet.2011.10.010.

14. Chintapalli, V. R., Bratty, M. Al, Korzekwa, D., Watson, D. G. & Dow, J. A. T. Mapping an Atlas of Tissue-Specific Drosophila melanogaster Metabolomes by High Resolution Mass Spectrometry. *PLoS One* **8**, 1–13 (2013).

15. Stephanopoulos, G. Metabolic Fluxes and Metabolic Engineering. *Metab. Eng.* **1**, 1–11 (1999).

16. Moxley, J. F. *et al.* Linking high-resolution metabolic flux phenotypes and transcriptional regulation in yeast modulated by the global regulator Gcn4p. *Proc. Natl. Acad. Sci. U. S. A.* **106**, 6477–6482 (2009).

17. Orth, J. D., Thiele, I. & Palsson, B. Ø. What is flux balance analysis ? *Nat. Publ. Gr.* **28**, 245–248 (2010).

18. Thiele, I. & Palsson, B. A protocol for generating a high-quality genome-scale metabolic reconstruction. *Nat. Protoc.* **5**, 93–121 (2010).

19. Wang, Y., Eddy, J. A. & Price, N. D. Reconstruction of genome-scale metabolic models for 126 human tissues using mCADRE. *BMC Syst. Biol.* (2012).

20. Shlomi, T., Berkman, O. & Ruppin, E. Regulatory on ̄off minimization of metabolic flux. **102**, (2005).

21. Safak Yilmaz, L. & Walhout, A. J. M. A Caenorhabditis elegans Genome-Scale Metabolic Network Model. *Cell Syst.* **2**, 297–311 (2016).

22. Chiappino-Pepe, A. & Hatzimanikatis, V. PhenoMapping: a protocol to map cellular phenotypes to metabolic bottlenecks, identify conditional essentiality, and curate metabolic models. *STAR Protoc.* **2**, 100280 (2021).

23. Schönborn, J. W., Jehrke, L., Mettler-Altmann, T. & Beller, M. FlySilico: Flux balance modeling of Drosophila larval growth and resource allocation. *Sci. Rep.* **9**, 1–16 (2019).

24. Cesur, M. F., Basile, A., Patil, K. R. & Çak, T. A new metabolic model of Drosophila melanogaster and the integrative analysis of Parkinson's disease. *Life Sci. Alliance* **6**, 1–21 (2023).

25. Wang, H. *et al.* Genome-scale metabolic network reconstruction of model animals as a platform for translational research. *Proc. Natl. Acad. Sci. U. S. A.* **118**, (2021).

26. Stephanopoulos;, G. N., Aristidou, A. A. & Nielsen, J. *Metabolic Engineering: Principles and Methodologies*. *Academic Press* vol. 1 (1998).

27. Antoniewicz, M. R. Using multiple tracers for 13C metabolic flux analysis. *Methods Mol. Biol.* **985**, 17–45 (2013).

28. Hensley, C. T. *et al.* Metabolic Heterogeneity in Human Lung Tumors. *Cell* **164**, 681–694 (2016).

29. Dong, W. *et al.* Oncogenic metabolic rewiring independent of proliferative control in human mammary epithelial cells. *bioRxiv* **2022.04.08**, 2022.04.08.486845 (2022).

30. Jang, C. *et al.* The Small Intestine Converts Dietary Fructose into Glucose and Organic Acids. *Cell Metab.* **27**, 351-361.e3 (2018).

31. Hui, S. *et al.* Quantitative Fluxomics of Circulating Metabolites. *Cell Metab.* **32**, 676-688.e4 (2020).

32. Hubbard, B. T. *et al.* Q-Flux: A method to assess hepatic mitochondrial succinate dehydrogenase, methylmalonyl-CoA mutase, and glutaminase fluxes in vivo. *Cell Metab.* **35**, 212-226.e4 (2023).

33. Jouandin, P. *et al.* Lysosomal cystine mobilization shapes the response of TORC1 and tissue growth to fasting. *Science (80-.).* **375**, (2022).

34. Henriques, S. F. *et al.* Metabolic cross-feeding in imbalanced diets allows gut microbes to improve reproduction and alter host behaviour. *Nat. Commun.* **11**, 1–15 (2020).

35. Parkhitko, A. A. *et al.* A genetic model of methionine restriction extends Drosophila health- and lifespan. 1–12 (2021) doi:10.1073/pnas.2110387118.

36. Agren, R. *et al.* Identification of anticancer drugs for hepatocellular carcinoma through personalized genome-scale metabolic modeling. *Mol. Syst. Biol.* **10**, 1–13 (2014).

37. Li, H. *et al.* Fly Cell Atlas: A single-nucleus transcriptomic atlas of the adult fruit fly. *Science (80-.).* **375**, (2022).

38. Wang, H. *et al.* RAVEN 2.0: A versatile toolbox for metabolic network reconstruction and a case study on Streptomyces coelicolor. *PLoS Comput. Biol.* **14**, 1–17 (2018).

39. Sartori, R., Romanello, V. & Sandri, M. Mechanisms of muscle atrophy and hypertrophy: implications in health and disease. *Nat. Commun.* **12**, 1–12 (2021).

40. Solmonson, A. & DeBerardinis, R. J. Lipoic acid metabolism and mitochondrial redox regulation.

J. Biol. Chem. **293**, 7522–7530 (2018).

41. Sánchez, B. J. *et al.* Improving the phenotype predictions of a yeast genome-scale metabolic model by incorporating enzymatic constraints. *Mol. Syst. Biol.* **13**, 935 (2017).

42. Lewis, J. E., Forshaw, T. E., Boothman, D. A., Furdui, C. M. & Kemp, M. L. Personalized Genome-Scale Metabolic Models Identify Targets of Redox Metabolism in Radiation-Resistant Tumors. *Cell Syst.* **12**, 68-81.e11 (2021).

43. Schwanhausse, B. *et al.* Global quantification of mammalian gene expression control. *Nature* **473**, 1–8 (2011).

44. Schomburg, I. *et al.* BRENDA, the enzyme database: Updates and major new developments. *Nucleic Acids Res.* **32**, 431–433 (2004).

45. Field, A. E. *et al.* DNA Methylation Clocks in Aging: Categories, Causes, and Consequences. *Mol. Cell* **71**, 882–895 (2018).

46. Gudmundsson, S. & Thiele, I. Computationally efficient flux variability analysis. *BMC Bioinformatics* **11**, 2–4 (2010).

47. Piper, M. D. W. *et al.* Matching Dietary Amino Acid Balance to the In Silico- Translated Exome Optimizes Growth and Reproduction without Cost to Lifespan Article Matching Dietary Amino Acid Balance to the In Silico-Translated Exome Optimizes Growth and Reproduction without Cost . *Cell Metab.* **25**, 610–621 (2017).

48. Ren, W. & Peng, Y. Betaine in inflammation : Mechanistic Aspects and Applications. **9**, 1–13 (2018).

49. Hadtstein, F. & Vrolijk, M. Vitamin B-6-Induced Neuropathy : Exploring the Mechanisms of Pyridoxine Toxicity. *Adv. Nutr.* **12**, 1911–1929 (2021).

50. Fustin, J. M. *et al.* Rhythmic Nucleotide Synthesis in the Liver: Temporal Segregation of Metabolites. *Cell Rep.* **1**, 341–349 (2012).

51. Chong, J. & Xia, J. Systems biology MetaboAnalystR : an R package for flexible and reproducible analysis of metabolomics data. *Bioinformatics* **34**, 4313–4314 (2018).

52. DeFronzo, R. A. & Tripathy, D. Skeletal muscle insulin resistance is the primary defect in type 2 diabetes. *Diabetes Care* **32 Suppl 2**, (2009).

53. Peralta, D. *et al.* A proton relay enhances H2O2 sensitivity of GAPDH to facilitate metabolic

adaptation. *Nat. Chem. Biol.* **11**, 156–163 (2015).

54. Reisz, J. A. *et al.* Oxidative modifications of glyceraldehyde 3-phosphate dehydrogenase regulate metabolic reprogramming of stored red blood cells GLUT. *Blood* **128**, e32–e42 (2016).

55. Dar, G. H. *et al.* GAPDH controls extracellular vesicle biogenesis and enhances the therapeutic potential of EV mediated siRNA delivery to the brain. *Nat. Commun.* **12**, (2021).

56. Dong, W., Moon, S. J., Kelleher, J. K. & Stephanopoulos, G. Dissecting Mammalian Cell Metabolism through 13 C- and 2 H - Isotope Tracing: Interpretations at the Molecular and Systems Levels. (2019) doi:10.1021/acs.iecr.9b05154.

57. Dong, W., Rawat, E. S., Stephanopoulos, G. & Abu-Remaileh, M. Isotope tracing in health and disease. *Curr. Opin. Biotechnol.* **76**, 102739 (2022).

58. Talwar, D. *et al.* The GAPDH redox switch safeguards reductive capacity and enables survival of stressed tumour cells. *Nat. Metab.* **5**, 660–676 (2023).

59. Vander Heiden, M. G. Targeting cancer metabolism: A therapeutic window opens. *Nat. Rev. Drug Discov.* **10**, 671–684 (2011).

60. Ido, Y. Pyridine nucleotide redox abnormalities in diabetes. *Antioxidants Redox Signal.* **9**, 931–942 (2007).

61. Silva, B. *et al.* Glia fuel neurons with locally synthesized ketone bodies to sustain memory under starvation. *Nat. Metab.* **4**, 213–224 (2022).

62. Al Batran, R. *et al.* Pimozide Alleviates Hyperglycemia in Diet-Induced Obesity by Inhibiting Skeletal Muscle Ketone Oxidation. *Cell Metab.* **31**, 909-919.e8 (2020).

63. Ferrer, M. *et al.* Cachexia: A systemic consequence of progressive, unresolved disease. *Cell* **186**, 1824–1845 (2023).

64. Wang, L. *et al.* Spatially resolved isotope tracing reveals tissue metabolic activity. *Nat. Methods* **19**, 223–230 (2022).

65. Robinson, J. L. *et al.* An atlas of human metabolism. *Sci. Signal.* **13**, 1–12 (2020).

66. Hu, Y. *et al.* An integrative approach to ortholog prediction for disease-focused and other functional studies. *BMC Bioinformatics* **12**, (2011).

67. Agren, R. *et al.* Reconstruction of genome-scale active metabolic networks for 69 human cell

types and 16 cancer types using INIT. *PLoS Comput. Biol.* **8**, (2012).

68. Petkova, M. D., Little, S. C., Liu, F. & Gregor, T. Maternal Origins of Developmental Reproducibility. *Curr. Biol.* **24**, 1283–1288 (2014).

69. Guet, C., Bruneaux, L., Min, T. L., Siegal-gaskins, D. & Figueroa, I. Minimally invasive determination of mRNA concentration in single living bacteria. *Nucleic Acids Res.* **36**, (2008).

70. Finka, A. & Goloubinoff, P. Proteomic data from human cell cultures refine mechanisms of chaperone-mediated protein homeostasis. *Cell Stress Chaperones* **18**, 591–605 (2013).

71. Wang, M., Herrmann, C. J., Simonovic, M. & Szklarczyk, D. Version 4 . 0 of PaxDb : Protein abundance data , integrated across model organisms , tissues , and cell-lines. 3163–3168 (2015) doi:10.1002/pmic.201400441.

72. Heiden, M. G. Vander *et al.* Understanding the Warburg Effect : Cell Proliferation. *Science (80-.).* **324**, 1029 (2009).

73. Hosios, A. M. & Matthew, G. V. H. The redox requirements of proliferating mammalian cells. *J. Biol. Chem.* **293**, 7490–7498 (2018).

74. Maddocks, O. D. *et al.* A roadmap for interpreting 13 C metabolite labeling patterns from cells. *Curr. Opin. Biotechnol.* **34**, 189–201 (2015).

75. Megchelenbrink, W., Huynen, M. & Marchiori, E. optGpSampler: An improved tool for uniformly sampling the solution-space of genome-scale metabolic networks. *PLoS One* **9**, (2014).

76. Väremo, L., Nielsen, J. & Nookaew, I. Enriching the gene set analysis of genome-wide data by incorporating directionality of gene expression and combining statistical hypotheses and methods. *Nucleic Acids Res.* **41**, 4378–4391 (2013).

77. Su, X., Lu, W. & Rabinowitz, J. D. Metabolite Spectral Accuracy on Orbitraps. *Anal. Chem.* **89**, 5940–5948 (2017).

78. Mirdita, M. *et al.* ColabFold: making protein folding accessible to all. *Nat. Methods* **19**, 679–682 (2022).

79. Jumper, J. *et al.* Highly accurate protein structure prediction with AlphaFold. *Nature* **596**, 583–589 (2021).

80. Kim, A.-R. *et al.* Enhanced Protein-Protein Interaction Discovery via AlphaFold-Multimer. *bioRxiv* 2024.02.19.580970 (2024).

81. Saavedra, P. *et al.* REPTOR/CREBRF encode key regulators of muscle energy metabolism. bioRxiv 2021.12.17.473012 (2023) doi:10.1038/s41467-023-40595-1.

82. Moon, S. J., Dong, W., Stephanopoulos, G. N. & Sikes, H. D. Oxidative pentose phosphate pathway and glucose anaplerosis support maintenance of mitochondrial NADPH pool under mitochondrial oxidative stress. *Bioeng. Transl. Med.* 1–18 (2020) doi:10.1002/btm2.10184.

83. Cracan, V., Titov, D. V., Shen, H., Grabarek, Z. & Mootha, V. K. A genetically encoded tool for manipulation of NADP+/NADPH in living cells. *Nat. Chem. Biol.* **13**, 1088–1095 (2017).

Figure legends

Fig 1. Reconstruction of tissue-specific metabolic models reveals distinct metabolic network structures and pathway coverage. a Tissue-specific genome-scale metabolic model reconstruction pipeline for *Drosophila*. **b** Metabolic network structures of 32 different tissues are compared using Hamming similarity method and represented in tSNE plot. **c** Heatmap describing the percent differences in metabolic pathway coverage across tissues. Number of reactions in each metabolic subsystem is calculated across tissues, and pathways with at least more than 100 % deviation from the mean coverage are shown. Metabolic subsystems of fat body and oenocytes are highlighted in the yellow box. **d** Comparison of the ability of the individual tissues to complete a total of 256 metabolic tasks. Z-scores were calculated based on the mean and standard deviation derived from the total number of completed tasks across all tissues.

Fig 2. Integration of enzyme kinetics and abundances reveals tissue-specific maximum rate distributions. a Calculation of V_{max} using available enzyme turnover number (k_{cat}) and enzyme abundances. **b** Scatter plot describing the distributions of V_{max} across the tissues. Each circle represents the log10 transformed V_{max} of individual reaction. The dashed line indicates the default maximum V_{max} value set in Fruitfly1. Tissues are sorted based on descending median V_{max} values, with darker red circles representing tissues with higher V_{max} and darker blue colors representing lower V_{max}. **c** Scatter plot showing the distribution of tissues with specific V_{max} and metabolic task.

Fig 3. Pathway flux variability highlights tissue-dependent metabolic similarities and differences. a Schematics representing flux balance, variability, and pathway variability analysis. **b** Heatmap showing the pathway flux variability, quantified as the sum of flux ranges of individual reactions in a pathway weighted by the total number of reactions. Z-scores were calculated based on the mean and standard deviation derived from the pathway flux variability across the tissues. Highlighted boxes represent tissues with high pathway flux variability of interest. **c - e** Heatmap showing the pathway flux variability across the selected pathways from the clustering analysis. Tissues with either high or low flux variability are shown are described. **f** t-SNE plot illustrating the distribution and clustering of tissues based on the pathway flux variability analysis. Each circle represents a tissue and is colored based on the assigned cluster.

Fig 4. Metabolite profiling supports tissue-specific pathway analyses. a. Experimental design describing the dissection of four major regions of *Drosophila* adult flies and liquid-chromatograph mass-spectrometry to profile around three hundred polar metabolites. Heatmap represents metabolite profiles across thorax, head, abdomen, and gut. **b.** Clustering of the metabolomics data set using principal component analysis. (n = 4 biological independent samples, with each replicate comprising 20 dissected body parts). **c-f** Boxplots representing the normalized peak area of selected metabolites across the dissected samples. The peak areas are normalized to the protein content of dissected samples. Welch's t-tests were used to calculate the p-values and adjusted using Bonferroni method to correct for multiple comparisons.

Fig 5. ^{13}C-isotope tracing and flux analysis identify GADPH as a rate-limiting enzyme in muscle under high sugar diet conditions. a Experimental design for measuring glycolysis activities using [U-$^{13}C_6$]glucose isotope tracers in response to high sugar diet. High sugar diet (HSD, 1 M sucrose) and normal sugar diet (NSD, 0.26 M sucrose) are made with supplementation of [U-$^{13}C_6$]glucose, keeping the same ratio of labeled to unlabeled carbons. **b** Isotope labeling pattern generated by [U-$^{13}C_6$]glucose in glycolysis. **c** Fractional enrichment of glycolytic intermediates. M+x denotes the mass increased by x number of carbons labeled with ^{13}C isotope. The horizontal bar represents the mean value, with error bars representing the standard deviation. Each dot represents individual datapoint (n = 6). Stars represent the significance. **d** Fractional enrichment of glycolysis intermediates, normalized to the M+6 glucose labeling fraction of either HSD or NSD conditions, respectively. **e** Isotope labeling pattern generated by the [U-$^{13}C_6$]glucose in the TCA cycle. **f** Fractional enrichment of TCA cycle intermediates. (n = 6). **g** Normalized fractional enrichment of TCA cycle metabolites. **h** Schematic representing the integration of ^{13}C labeling patterns and experimentally measured glucose uptake rates as constraints for flux balance analysis. **i** Flux prediction in response to HSD. The numbers next to the arrow represent the predicted flux magnitude, and the minimum and maximum values are denoted in parenthesis. **j** Schematic representing the GAPDH reaction, and the potential source of NAD^+ and NADH by lactate dehydrogenase and aldehyde dehydrogenase reactions, respectively. **k** Perturbation effect analysis for glycolytic enzymes. The maximum rates of individual reactions were reduced by 10 % and the change of total reaction rates in glycolysis were calculated. **l** Fraction of NADH and NAD^+ relative to the total NAD(H) pool and the NADH/NAD^+ ratio. **m-n** Distribution of predicted fluxes in **(m)** lactate dehydrogenase, and **(n)** glycerol-3-phosphate dehydrogenase. Flux sampling analysis was used after the flux variability analysis, with 10,000 simulations for each condition. **o** Pie charts representing the relative proportions of GPDH and LDH rates under NSD (left) and HSD (right) conditions. **p** Schematic representing the contribution of [U-

$^{13}C_6$]glucose to glycerol-3-phosphate and lactate. **q** The ratio between the fractional labeling of M+3 G3P and that of M+3 lactate.

Fig 6. Pathway flux index analysis identifies altered fructose and butanoate metabolism in muscle under HSD. a Pathway flux index is defined to estimate metabolic pathway activities based on flux range and mean of individual reaction rates obtained in each pathway. **b** Comparison of pathway flux index between HSD and NSD across metabolic pathways. **c** Simulated flux distribution in conversion of fructose to fructose-6-phosphate in response to HSD (red) or NSD (black) (n_{sim} = 10,000). **d** Simulated flux distribution in conversion of 3-hydroxybutyrate to acetoacetate in response to HSD (red) or NSD (black) (n_{sim} = 10,000). **e** Schematic representing the targeted metabolite profiling of thorax for w^{1118} male flies fed in high (1 M) or normal (0.26 M) sugar diet for five days. **f** volcano plot representing the significantly altered metabolites in thorax in response to HSD. Each dot represents a metabolite, with the x-axis showing the fold change and the y-axis displaying the p-value. Metabolites above the significance thresholds are highlighted in blue (enriched in NSD), or red (enriched in HSD). **g-h** Relative change of metabolites and predicted fluxes in **(g)** fructose and **(h)** butanoate metabolic pathways. Metabolites are highlighted to the color based on the log2 fold change of metabolites between HSD and NSD (HSD/NSD). The relative change of sucrose/trehalose, sorbitol, and acetoacetyl-CoA against the diets are shown in boxplots. Arrows represent the reaction steps with colors indicating the log2 fold change of predicted rate between HSD and NSD. Boxplots representing the normalized peak area of selected metabolites under HSD and NSD. Welch's t-tests were used to calculate the p-values.

a

Reconstruction of tissue-specific genome-scale metabolic models pipeline

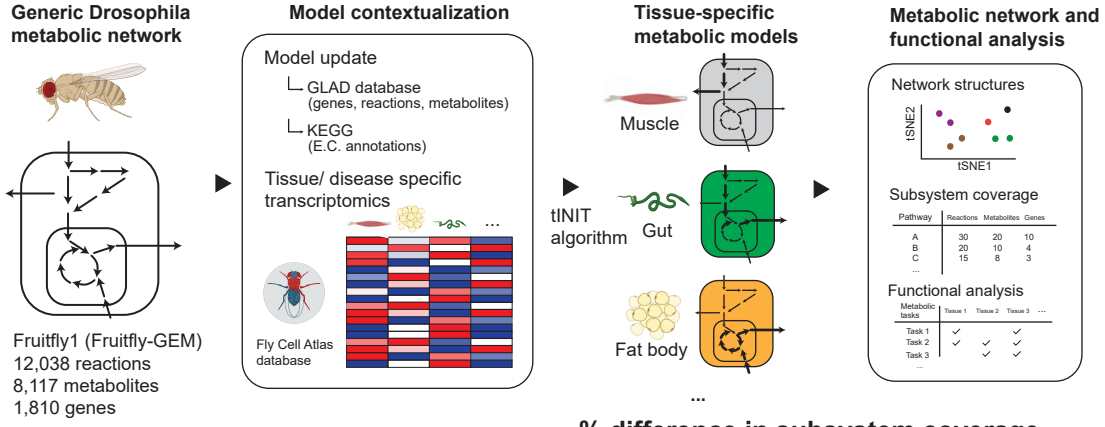

b

Comparison of metabolic network structures

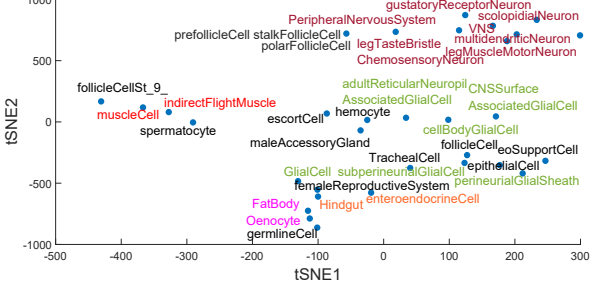

c

% difference in subsystem coverage

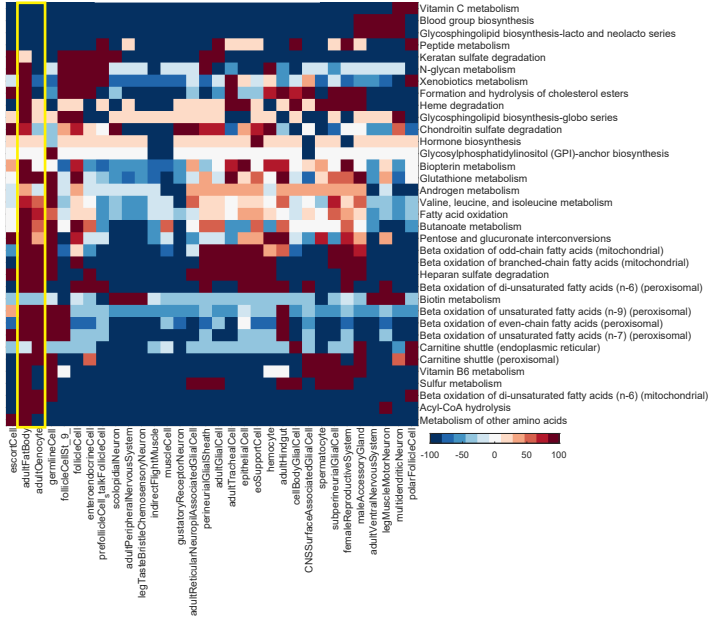

d

Ability to complete metabolic tasks

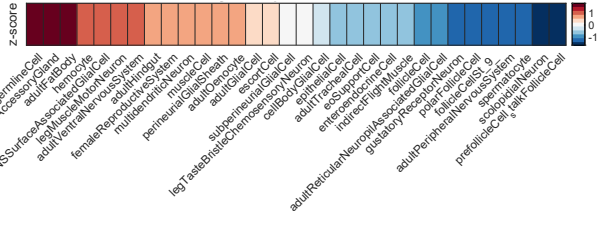

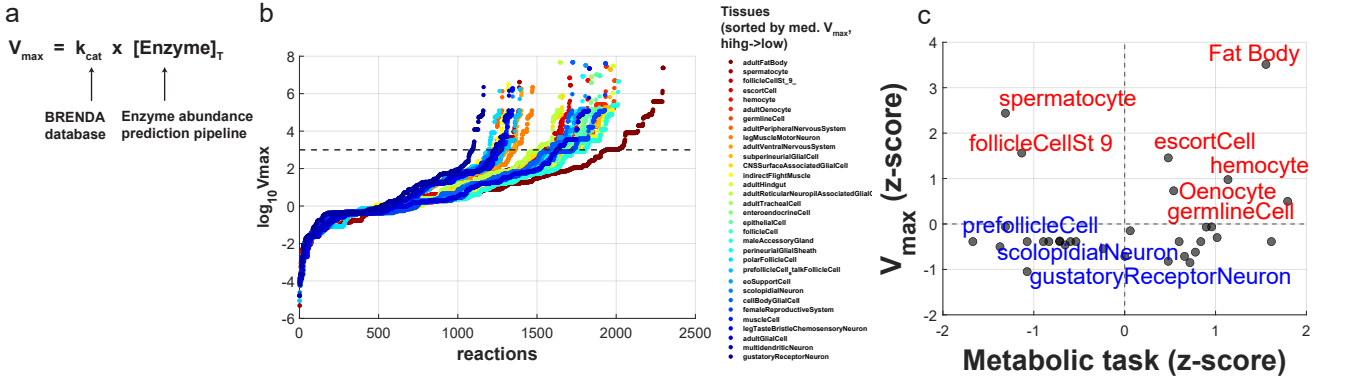
a
$V_{max} = k_{cat} \times [Enzyme]_T$
BRENDA database
Enzyme abundance prediction pipeline
b
$\log_{10}$ Vmax
reactions
Tissues (sorted by med. V_{max}, hihg->low)
adultFatBody
spermatocyte
follicleCellSt_9_
escortCell
hemocyte
adultOenocyte
germlineCell
adultPeripheralNervousSystem
legMotorNeuron
adultVentralNervousSystem
subperineurialGlialCell
CNSSurfaceAssociatedGlialCell
indirectFlightMuscle
adultHindgut
adultRetrocerebralNeurosecretoryGlialC
adultTrachealCell
enteroendocrineCell
epithelialCell
follicleCell
maleAccessoryGland
perineurialGlialSheath
polarFollicleCell
prefollicleCell_tailFollicleCell
eoSupportCell
scolopidialNeuron
cellBodyGlialCell
femaleReproductiveSystem
muscleCell
legTasteBristleChemosensoryNeuron
adultGlialCell
multidendriticNeuron
gustatoryReceptorNeuron
c
V_{max} (z-score)
Metabolic task (z-score)
Fat Body
spermatocyte
follicleCellSt 9
escortCell
hemocyte
Oenocyte
germlineCell
prefollicleCell
scolopidialNeuron
gustatoryReceptorNeuron

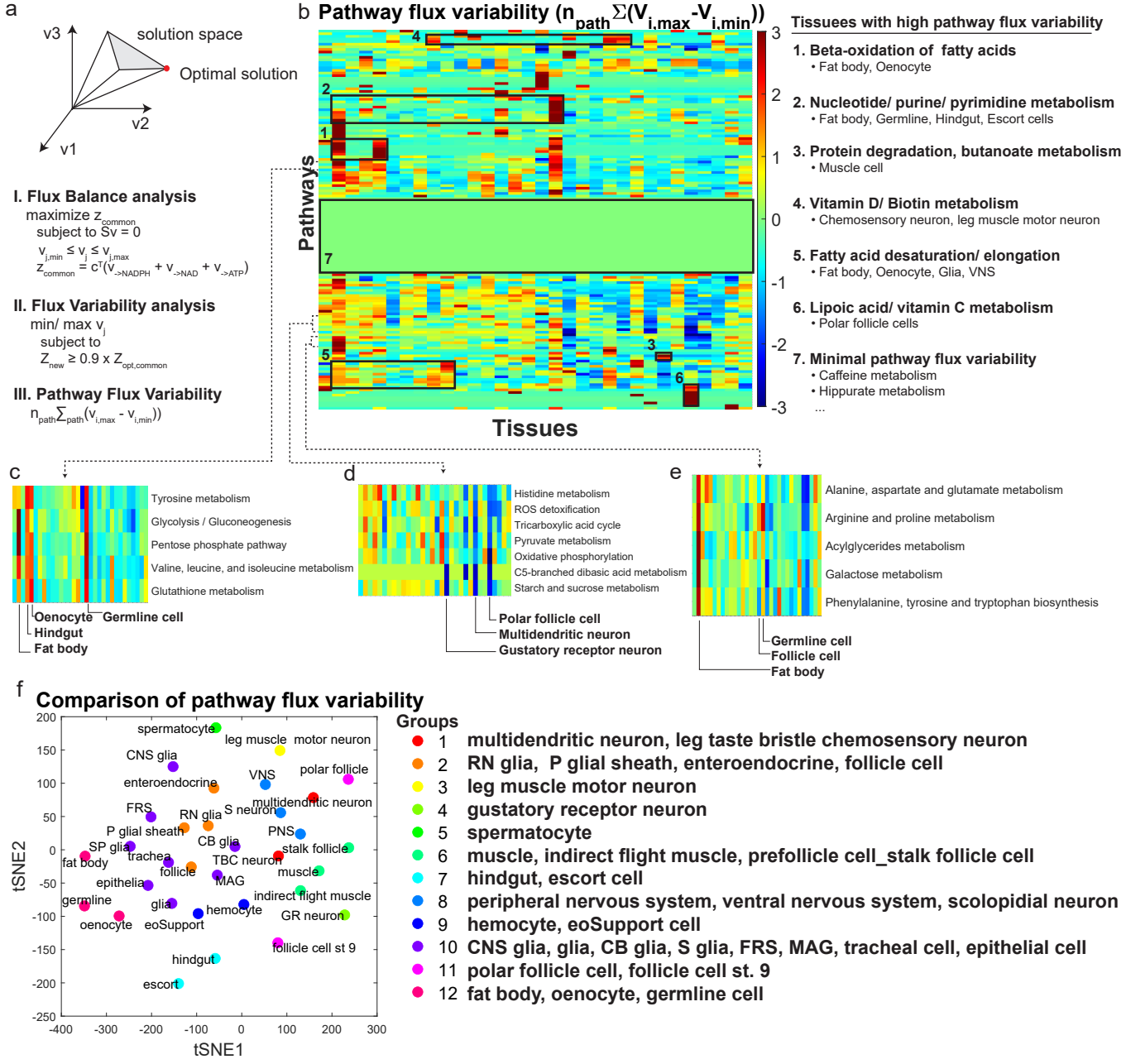
a
v3
solution space
Optimal solution
v2
v1
I. Flux Balance analysis
maximize z_{common}
subject to $Sv = 0$
$v_{j,min} \le v_j \le v_{j,max}$
$z_{common} = c^T(v_{->NADPH} + v_{->NAD} + v_{->ATP})$
II. Flux Variability analysis
min/ max v_j
subject to
$Z_{new} \ge 0.9 \times Z_{opt,common}$
III. Pathway Flux Variability
$n_{path}\sum_{path}(v_{i,max} - v_{i,min})$
b Pathway flux variability ($n_{path}\Sigma(V_{i,max}-V_{i,min})$)
Pathways
Tissues
1
2
3
4
5
6
7
3
2
1
0
-1
-2
-3
Tissuees with high pathway flux variability
1. Beta-oxidation of fatty acids
• Fat body, Oenocyte
2. Nucleotide/ purine/ pyrimidine metabolism
• Fat body, Germline, Hindgut, Escort cells
3. Protein degradation, butanoate metabolism
• Muscle cell
4. Vitamin D/ Biotin metabolism
• Chemosensory neuron, leg muscle motor neuron
5. Fatty acid desaturation/ elongation
• Fat body, Oenocyte, Glia, VNS
6. Lipoic acid/ vitamin C metabolism
• Polar follicle cells
7. Minimal pathway flux variability
• Caffeine metabolism
• Hippurate metabolism
...
c
Tyrosine metabolism
Glycolysis / Gluconeogenesis
Pentose phosphate pathway
Valine, leucine, and isoleucine metabolism
Glutathione metabolism
Oenocyte
Germline cell
Hindgut
Fat body
d
Histidine metabolism
ROS detoxification
Tricarboxylic acid cycle
Pyruvate metabolism
Oxidative phosphorylation
C5-branched dibasic acid metabolism
Starch and sucrose metabolism
Polar follicle cell
Multidendritic neuron
Gustatory receptor neuron
e
Alanine, aspartate and glutamate metabolism
Arginine and proline metabolism
Acylglycerides metabolism
Galactose metabolism
Phenylalanine, tyrosine and tryptophan biosynthesis
Germline cell
Follicle cell
Fat body
f
Comparison of pathway flux variability
tSNE2
tSNE1
200
150
100
50
0
-50
-100
-150
-200
-250
-400
-300
-200
-100
0
100
200
300
spermatocyte
leg muscle
motor neuron
CNS glia
polar follicle
VNS
enteroendocrine
multidendritic neuron
FRS
RN glia
S neuron
P glial sheath
PNS
SP glia
CB glia
stalk follicle
fat body
trachea
TBC neuron
follicle
muscle
epithelia
MAG
germline
indirect flight muscle
glia
hemocyte
GR neuron
oenocyte
eoSupport
follicle cell st 9
hindgut
escort
Groups
1 multidendritic neuron, leg taste bristle chemosensory neuron
2 RN glia, P glial sheath, enteroendocrine, follicle cell
3 leg muscle motor neuron
4 gustatory receptor neuron
5 spermatocyte
6 muscle, indirect flight muscle, prefollicle cell_stalk follicle cell
7 hindgut, escort cell
8 peripheral nervous system, ventral nervous system, scolopidial neuron
9 hemocyte, eoSupport cell
10 CNS glia, glia, CB glia, S glia, FRS, MAG, tracheal cell, epithelial cell
11 polar follicle cell, follicle cell st. 9
12 fat body, oenocyte, germline cell

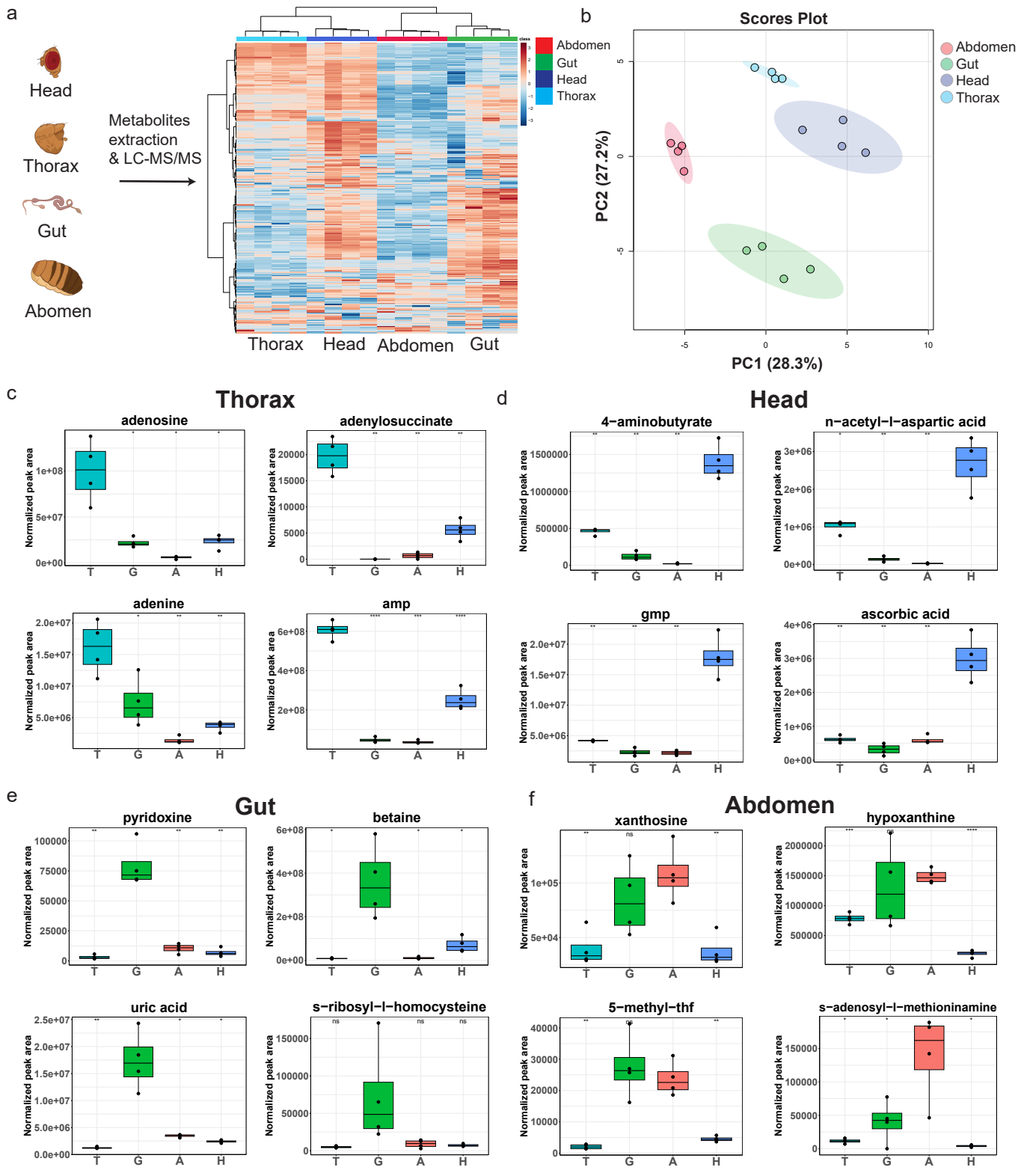
a
Head
Thorax
Gut
Abomen
Metabolites extraction & LC-MS/MS
Thorax
Head
Abdomen
Gut
Abdomen
Gut
Head
Thorax
b
Scores Plot
PC2 (27.2%)
PC1 (28.3%)
Abdomen
Gut
Head
Thorax
c
Thorax
adenosine
adenylosuccinate
adenine
amp
Normalized peak area
T
G
A
H
d
Head
4−aminobutyrate
n−acetyl−l−aspartic acid
gmp
ascorbic acid
e
Gut
pyridoxine
betaine
uric acid
s−ribosyl−l−homocysteine
f
Abdomen
xanthosine
hypoxanthine
5−methyl−thf
s−adenosyl−l−methioninamine

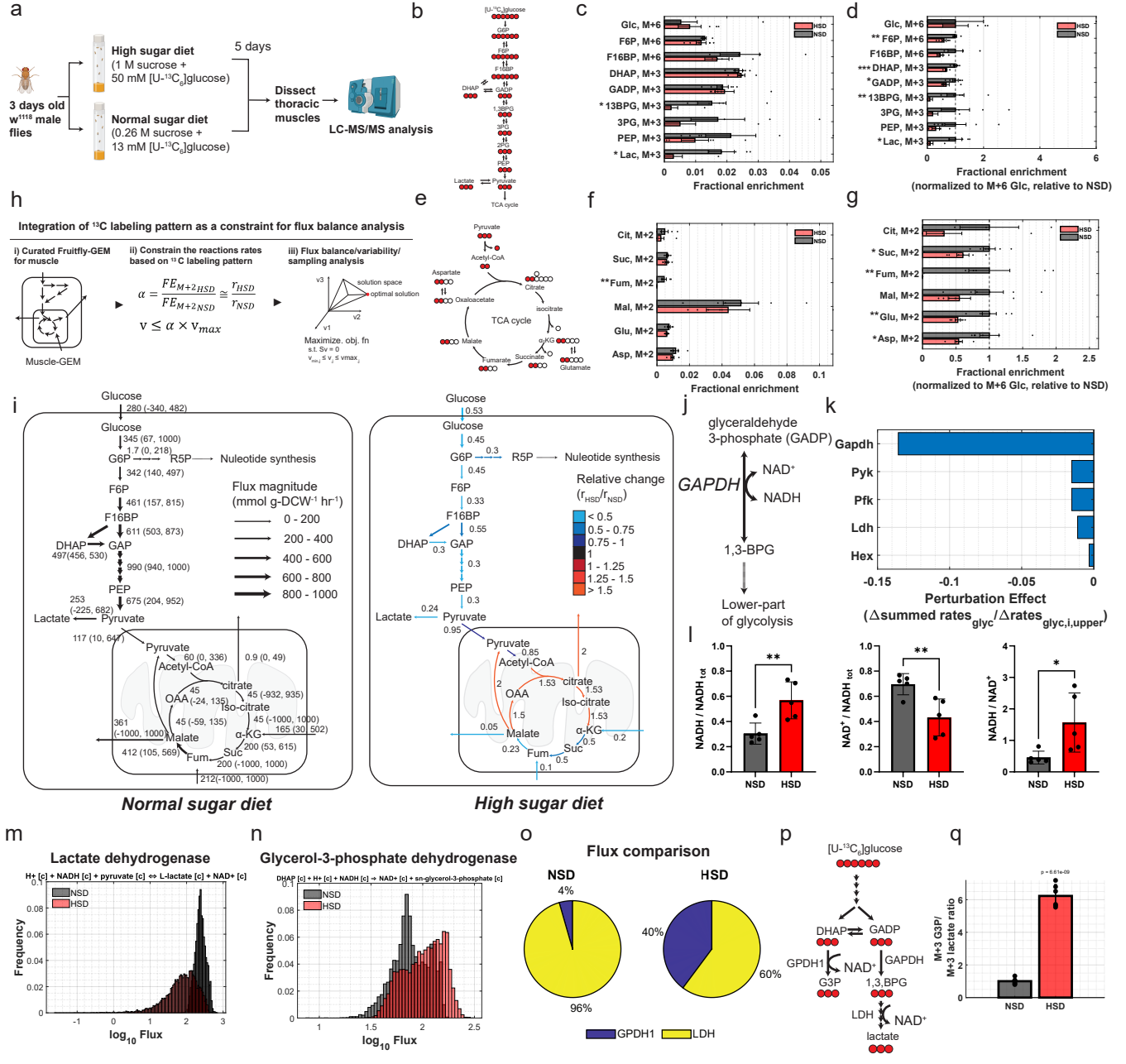
a
3 days old w1118 male flies
High sugar diet
(1 M sucrose + 50 mM [U-13C6]glucose)
Normal sugar diet
(0.26 M sucrose + 13 mM [U-13C6]glucose)
5 days
Dissect thoracic muscles
LC-MS/MS analysis
b
[U-13C6]glucose
G6P
F6P
F16BP
DHAP
GADP
1,3BPG
3PG
2PG
PEP
Lactate
Pyruvate
TCA cycle
c
Glc, M+6
F6P, M+6
F16BP, M+6
DHAP, M+3
GADP, M+3
* 13BPG, M+3
3PG, M+3
PEP, M+3
* Lac, M+3
HSD
NSD
Fractional enrichment
d
Glc, M+6
** F6P, M+6
F16BP, M+6
*** DHAP, M+3
* GADP, M+3
** 13BPG, M+3
3PG, M+3
PEP, M+3
* Lac, M+3
Fractional enrichment
(normalized to M+6 Glc, relative to NSD)
h
Integration of 13C labeling pattern as a constraint for flux balance analysis
i) Curated Fruitfly-GEM for muscle
Muscle-GEM
ii) Constrain the reactions rates based on 13C labeling pattern
iii) Flux balance/variability/ sampling analysis
solution space
optimal solution
Maximize. obj. fn
s.t. Sv = 0
e
Pyruvate
Acetyl-CoA
Aspartate
Oxaloacetate
Citrate
isocitrate
TCA cycle
Malate
α-KG
Fumarate
Succinate
Glutamate
f
Cit, M+2
Suc, M+2
** Fum, M+2
Mal, M+2
Glu, M+2
Asp, M+2
Fractional enrichment
g
Cit, M+2
* Suc, M+2
** Fum, M+2
Mal, M+2
** Glu, M+2
* Asp, M+2
Fractional enrichment
(normalized to M+6 Glc, relative to NSD)
i
Glucose
280 (-340, 482)
345 (67, 1000)
1.7 (0, 218)
G6P
R5P
Nuleotide synthesis
342 (140, 497)
F6P
461 (157, 815)
F16BP
611 (503, 873)
DHAP
GAP
497(456, 530)
990 (940, 1000)
PEP
253 (-225, 682)
675 (204, 952)
Lactate
Pyruvate
117 (10, 647)
Flux magnitude (mmol g-DCW-1 hr-1)
0 - 200
200 - 400
400 - 600
600 - 800
800 - 1000
Pyruvate
60 (0, 336)
0.9 (0, 49)
Acetyl-CoA
citrate
45 (-24, 135)
45 (-932, 935)
OAA
Iso-citrate
45 (-59, 135)
45 (-1000, 1000)
165 (30, 502)
361 (-1000, 1000)
Malate
α-KG
412 (105, 569)
Fum
Suc
200 (53, 615)
200 (-1000, 1000)
212(-1000, 1000)
Normal sugar diet
Glucose
0.53
0.45
0.3
0.45
0.33
0.55
0.3
0.3
0.24
0.95
Relative change (rHSD/rNSD)
< 0.5
0.5 - 0.75
0.75 - 1
1
1 - 1.25
1.25 - 1.5
> 1.5
2
1.53
1.5
0.05
0.23
0.85
0.2
0.5
0.1
High sugar diet
j
glyceraldehyde 3-phosphate (GADP)
GAPDH
NAD+
NADH
1,3-BPG
Lower-part of glycolysis
k
Gapdh
Pyk
Pfk
Ldh
Hex
Perturbation Effect
(Δsummed rates glyc / Δrates glyc,i,upper)
l
NADH / NADHtot
NAD+ / NADHtot
NADH / NAD+
NSD
HSD
m
Lactate dehydrogenase
H+ [c] + NADH [c] + pyruvate [c] ⇔ L-lactate [c] + NAD+ [c]
Frequency
log10 Flux
n
Glycerol-3-phosphate dehydrogenase
DHAP [c] + H+ [c] + NADH [c] → NAD+ [c] + sn-glycerol-3-phosphate [c]
Frequency
log10 Flux
o
Flux comparison
NSD
4%
96%
HSD
40%
60%
GPDH1
LDH
p
[U-13C6]glucose
DHAP
GADP
GPDH1
NAD+
GAPDH
G3P
1,3,BPG
LDH
NAD+
lactate
q
p = 6.61e-09
M+3 G3P/ M+3 lactate ratio
NSD
HSD

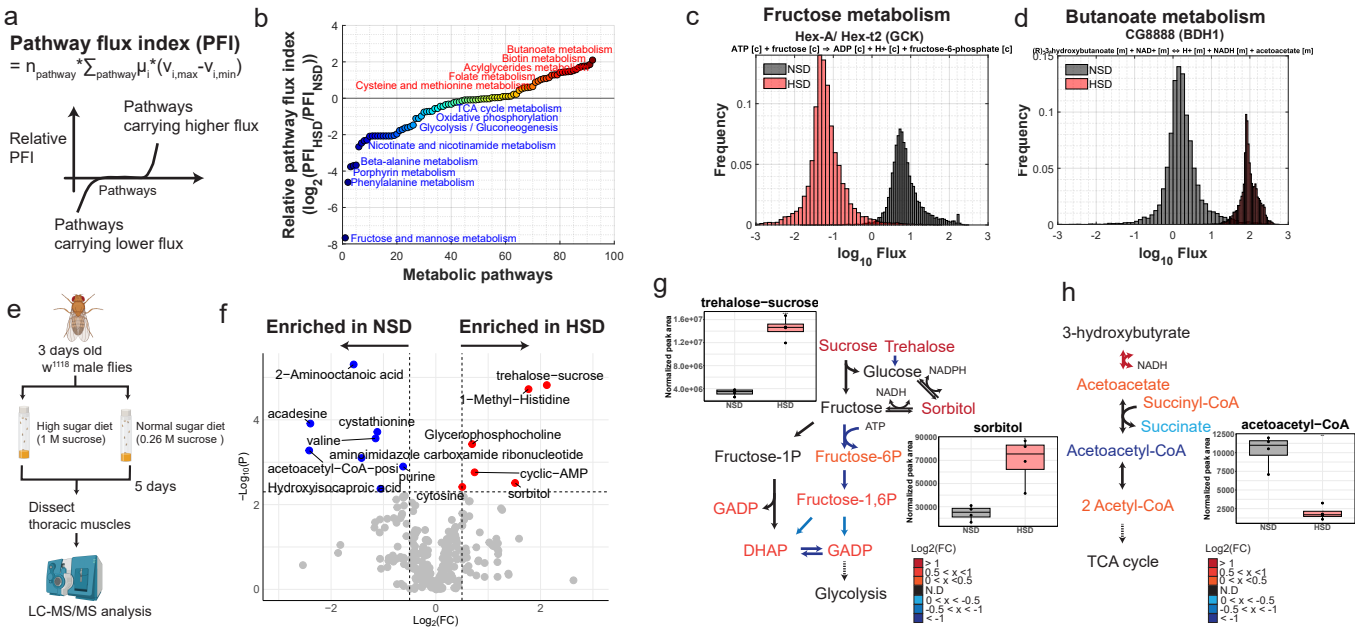
a
Pathway flux index (PFI)
= n_pathway*∑_pathway μ_i*(v_i,max-v_i,min)
Relative PFI
Pathways carrying higher flux
Pathways
Pathways carrying lower flux
b
Relative pathway flux index (log2(PFI_HSD/PFI_NSD))
Metabolic pathways
Butanoate metabolism
Biotin metabolism
Acylglycerides metabolism
Folate metabolism
Cysteine and methionine metabolism
CA cycle metabolism
Oxidative phosphorylation
Glycolysis / Gluconeogenesis
Nicotinate and nicotinamide metabolism
Beta-alanine metabolism
Porphyrin metabolism
Phenylalanine metabolism
Fructose and mannose metabolism
c
Fructose metabolism
Hex-A/ Hex-t2 (GCK)
ATP [c] + fructose [c] → ADP [c] + H+ [c] + fructose-6-phosphate [c]
NSD
HSD
Frequency
log10 Flux
d
Butanoate metabolism
CG8888 (BDH1)
(R)-3-hydroxybutanoate [m] + NAD+ [m] ⇔ H+ [m] + NADH [m] + acetoacetate [m]
NSD
HSD
Frequency
log10 Flux
e
3 days old w1118 male flies
High sugar diet (1 M sucrose)
Normal sugar diet (0.26 M sucrose)
5 days
Dissect thoracic muscles
LC-MS/MS analysis
f
Enriched in NSD
Enriched in HSD
2−Aminooctanoic acid
acadesine
cystathionine
valine
aminoimidazole carboxamide ribonucleotide
acetoacetyl−CoA−pos
purine
Hydroxyisocaproic acid
cytosine
Glycerophosphocholine
trehalose−sucrose
1−Methyl−Histidine
cyclic−AMP
sorbitol
−Log10(P)
Log2(FC)
g
trehalose−sucrose
Normalized peak area
NSD
HSD
Sucrose
Trehalose
Glucose
NADPH
NADH
Fructose
Sorbitol
ATP
Fructose-1P
Fructose-6P
Fructose-1,6P
GADP
DHAP
GADP
Glycolysis
sorbitol
Normalized peak area
NSD
HSD
Log2(FC)
> 1
0.5 < x <1
0 < x <0.5
N.D
0 < x < -0.5
-0.5 < x < -1
< -1
h
3-hydroxybutyrate
NADH
Acetoacetate
Succinyl-CoA
Succinate
Acetoacetyl-CoA
2 Acetyl-CoA
TCA cycle
acetoacetyl−CoA
Normalized peak area
NSD
HSD
Log2(FC)
> 1
0.5 < x <1
0 < x <0.5
N.D
0 < x < -0.5
-0.5 < x < -1
< -1